ELECTRONIC DEVICE FABRICATION AND CHARACTERIZATION BASED ON TWO-DIMENSIONAL MATERIALS

BY

ZHENGFENG YANG

THESIS

Submitted in partial fulfillment of the requirements
for the degree of Master of Science in Electrical and Computer Engineering
in the Graduate College of the
University of Illinois at Urbana-Champaign, 2017

Urbana, Illinois

Adviser:

Assistant Professor Wenjuan Zhu

Abstract

Two-dimensional (2D) materials have attracted extensive attention due to their unique and remarkable properties, such as the atomically thin body, pristine surface free of dangling bonds, tunable bandgap, and reasonably high mobility, which make 2D materials promising candidates for novel electronic and optoelectronic devices in low power, high performance and flexible applications.

In this thesis, the optical and electrical properties of MoS_2/WS_2 heterostructures grown by chemical vapor deposition (CVD) are studied. By using Raman spectra, photoluminescence (PL) spectra and atomic force microscopy (AFM), the vertical and lateral MoS_2/WS_2 structures are identified. The transistors and Hall-bar devices based on vertical monolayer-MoS_2/monolayer-WS_2 heterostructures are successfully fabricated. The devices show typical n-channel characteristics, indicating that MoS_2 and WS_2 are naturally n-type doped. Further investigation of the interlayer coupling on carrier transport and distribution is needed in future study. Due to the type II band alignment and sharp interface, these vertical and lateral MoS_2/WS_2 heterostructures can potentially be used for tunneling field-effect transistors and high-speed photodetectors.

In addition, the crystal orientation and electronic transport in germanium selenide (GeSe) are also studied. The crystallographic direction of the GeSe is determined by angle-resolved polarized Raman measurement. The anisotropic electronic transport of the GeSe is measured by angle-resolved DC electrical conductance. The results indicate that GeSe has a prominent anisotropic electronic transport with maximum conductance likely along the armchair direction, but further confirmation with repeatable experimental results is needed. The anisotropic conductance in GeSe may enable a new series of electronic and optoelectronic devices such as plasmonic devices with resonance

frequency continuously tunable with light polarization direction, and high-efficiency thermoelectric devices.

In summary, the MoS_2/WS_2 heterostructures and anisotropic electronic transport in GeSe have been studied. The knowledge gained in these projects will be essential for designing and fabricating novel electronic devices based on these materials in the future.

DEDICATED

To:

My beloved family

Whose consistent support and love made it possible for me to complete this work and my degrees,

And to:

My best friends

Whose help and encouragement made it possible for me to walk through the dark valley of my life.

Contents

Chapter 1 Introduction

In the past few decades, semiconductor technologies have been advanced generation by generation through device scaling. The semiconductor industry is touching the 10nm node technology and the prosperous development of modern electronic devices drives the scaling down to even smaller dimensions with faster speed, reduced cost and lower power consumption. Approaching the end of Moore's law, the miniaturization of metal-oxide-semiconductor field-effect-transistor (MOSFET) is facing severe challenges. Scaling the channel length down to sub-10nm regime will cause drain-induced barrier lowering, roll-off of the threshold voltage and hot carrier effect, which will substantially degrade the performance of the devices. As the scaling approaches its fundamental and technical limits, the semiconductor industry calls for innovations that can either extend the scaling or go beyond scaling.

In the context of exploring solutions and developing a new generation of electronics (e.g. flexible electronics), researchers have been looking for alternative materials and new device configurations [1] to sustain Moore's law and replace the dominant position of current Si technology. Among new candidate materials, two-dimensional (2D) materials emerged in recent years as promising candidates, which may be able to address some of these challenges with their unique properties.

1.1 The Properties of Two-dimensional Materials

First of all, the atomically thin body in 2D materials [2, 3], as illustrated in Figure 1.1, can potentially extend the scaling beyond 10nm technology. For planar structure transistors, the characteristic channel scaling length is given by $\lambda = \sqrt{t_{ox} t_s \varepsilon_s / \varepsilon_{ox}}$, where t_{ox} and t_s are the thickness of gate insulator and semiconductor, and ε_{ox} and ε_s are the permittivity of gate insulator and semiconductor [4]. With the atomically thin body down to less than 1nm in

single layer of 2D materials, the characteristic length could possibly be scaled down to smaller than 5nm. Thus, 2D materials are immune to short channel effects and thereby provide a viable path for electronics to sustain Moore's law.

Moreover, as the atomic structures in Figure 1.1 illustrate, the pristine surface with absence of the surface dangling bonds gives 2D materials significant advantages of less carrier scattering and interface states over the conventional bulk materials, thus leading to potentially higher performance in electrical and optical devices based on 2D materials [5].

2D materials are layered materials with strong in-plane covalent bond and weak interlayer van der Waals force. The weak interlayer bonding enables 2D materials to be easily exfoliated layer by layer. In addition, as shown in Figure 1.2 these layered materials can also be stacked up easily to build heterostructures in random orders as desired just like playing with Lego blocks. What is more, it has been predicted [6] that there are more than a hundred 2D materials in nature with diverse materials properties ranging from conductors (e.g., graphene), to semiconductors (e.g., transition metal dichalcogenides) to insulators (e.g., boron nitride). Thus, they provide diverse platforms to build various electronic and optical devices as required in the applications, and the issue of lattice mismatch is not a concern in the construction of 2D material heterostructures, unlike in bulk material heterostructures [7].

In addition to the properties above, the sheet-like flexibility enables 2D materials to sustain relatively high strains [8, 9] and therefore 2D materials are ideal candidate materials for future flexible electronics [10, 11]. The high surface-to-volume ratio also gives 2D materials the benefit of sensitive surfaces that could be used for highly sensitive sensors [12, 13]. With these unique and excellent properties, 2D materials have attracted extensive attention since their emergence. In the following, the specific properties and applications of graphene and transition metal dichalcogenides will be discussed in detail.

1.2 Graphene

Graphene is the first 2D material that has been extensively studied. In 2001, Novoselov and Geim in the UK found that single-layer graphene can be mechanically exfoliated from bulk graphite [14]. This gave the researcher access to the atomically thin 2D materials in the lab for the first time. Since then, 2D materials have attracted intense research interest. Figure 1.3 (a) [15] shows the energy dispersion of graphene. Its conduction band meets the valence band at the Dirac point and thus the bandgap of graphene is zero. With this unique electronic structure graphene has superior electron and hole mobility up to 15,000 $cm^2/(V•s)$ [16]. With the remarkably high carrier mobility graphene is promising for high-speed radio frequency electronics and plasmonic devices. In addition, it was found that graphene only absorbs 2.3% of incident visible light [17]. Therefore, graphene exhibits a promising application as a semi-metallic material and transparent conductor. Moreover, graphene can be easily and continuously tuned to be n-type or p-type without degradation of mobility by shifting the Fermi level with changing gate bias [18]. This ambipolar electric field effect meets the requirement in various applications that need the materials to be semiconducting n-type or p-type with different carrier concentrations.

However, the absence of bandgap in graphene limits its application in logic devices [19]. As Figure 1.4 illustrates, the transfer characteristics of a graphene transistor show a very high off-state current around 10 μA with 0.1V drain voltage. This high off-state current makes it impossible for graphene-based logic devices to turn off. Bilayer graphene has been reported to provide a bandgap, but the bandgap is very small (typically less than 0.2eV) [20]. Graphene nanoribbons could open up a bandgap due to the quantum confinement and edge effects, and it is theoretically and experimentally verified that the gap scales up with decreasing width of graphene nanoribbons [21, 22]. However, the mobility in graphene nanoribbons is typically significantly degraded, when the width of the ribbon reduces due to the edge roughness [23]. Thus, the absence of band gap brings challenges in the applications of graphene in logic devices.

1.3 Transition Metal Dichalcogenides

1.3.1 Material Properties of TMDs

For the application in logic devices, the channel material must have a sizable bandgap to ensure the required on-off current ratio. Beyond graphene, other 2D materials, such as transition metal dichalcogenides (TMDs) (e.g., MoS_2, WS_2, $MoSe_2$, etc.), with appreciable bandgap have attracted intense interest in the last few years as potential choices for logic devices [24, 25]. Among TMDs, MoS_2 has drawn the most attention. As Figure 1.1 (b) [3] demonstrates, the thickness of single layer of MoS_2, consisting of one layer of Mo atoms sandwiched by two layer of S atoms, is 6.5 Å.

Figure 1.3 (b) illustrates the evolution of MoS_2 band structures from bulk, quadrilayer, bilayer and monolayer from left to right [26]. The bulk MoS_2 is a semiconducting material with an indirect bandgap of 1.2 eV. Its conduction band minimum is located at the midpoint along the line of Γ-K while its valence band maximum is at the Γ point, which results in the indirect bandgap. As the material is thinned from bulk down to monolayer, the band structures change dramatically and the size of bandgap scales up as in Figure 1.5 (a) [27] where the monolayer MoS_2 has a bandgap of 1.9 eV. The quantum confinement effects lead to the transition of indirect-direct bandgap from bulk to monolayer. Due to valence band maximum and conduction band minimum seating at the same K-point, the monolayer has a direct bandgap with which monolayer MoS_2 demonstrates significantly enhanced photoluminescence (PL) as in Figure 1.5 (b). More importantly, it opens up the possibility of monolayer MoS_2 in the applications of light emission [28].

For the applications in digital devices, the sizable bandgap enables MoS_2 to have an enormous advantage over graphene. As Figure 1.6 demonstrates, the off-state current of monolayer MoS_2 transistor is around 10 pA, which is one millionth the size of a graphene transistor as illustrated in Figure 1.4, although the on/off ratio, extracted field-effect mobility and subthreshold swing from the Id-Vg

curve of monolayer MoS_2 transistor are far from the level that is used for current digital applications, which is also a big topic in improving the MoS_2 based device performance in the research community. With the off-state current of 10 pA and even smaller, the MoS_2 transistor would be turned off and more energy efficient.

In addition, the unique physical, mechanical, electrical, optical, and chemical properties of 2D materials can potentially enable novel electronic and photonic devices such as vertical tunnel transistors, photodetectors, solar cells, and flexible electronics [16, 24, 29], as discussed in the following.

1.3.2 TMDs-based Devices

Electronic Devices

Theoretical study predicted that the mobility of monolayer MoS_2 could reach a few thousand $cm^2V^{-1}s^{-1}$ at room temperature and even exceed 100,000 $cm^2V^{-1}s^{-1}$ at low temperature, depending on the charge impurity density and surrounding dielectric environment [30, 31]. In experiment, the mobility of MoS_2 in different layers was measured by using a van der Waals heterostructure and encapsulating MoS_2 within boron nitride (BN). The study confirmed that the mobility of MoS_2 was limited by extrinsic interfacial impurities and the mobility of six-layer MoS_2 reached 34,000 $cm^2V^{-1}s^{-1}$ at low temperature [32]. The study proves that MoS_2 has potentially have high enough mobility for high-performance electronics, although most of the experimental data give a few hundred mobility values or even lower [33, 34], mainly limited by dielectric materials, charged impurities and contact resistance.

In ultra-thin-body (UTB) semiconductors, the decreasing body thickness with dangling bonds and surface roughness results in carrier scattering and thus greatly decreased mobility [5]. However, the pristine surface with the absence of dangling bonds in 2D materials is beneficial for reduced interface states and carrier scattering. And in FETs with 2D TMDs materials as the channel, the

carriers are confined in the atomically thin body of 2D TMDs materials and the gate would control the channel uniformly and lead to better gate coupling.

Moreover, digital electronic devices require a large bandgap, usually greater than 1 eV, to achieve high on/off ratios [24]. The bandgaps of 2D TMDs are sufficiently large, indicating that electronic devices with 2D TMDs as the channels may achieve high on/off ratios.

Single layer MoS_2 field-effect transistors (FETs) have been extensively studied. Top-gated single layer MoS_2 field-effect transistors demonstrated large on/off ratios (~10^8) and low subthreshold swings (~74 mV/dec) [3] and bottom-gated unencapsulated single layer MoS_2 field-effect transistors gave moderate mobility (> 60 $cm^2V^{-1}s^{-1}$) at room temperature with on/off ratios of 10^5, as illustrated in Figure 1.7 (a) [35]. In 2015, single layer WS_2 FETs sandwiched between BN with Al/Au contact were reported to have high mobility of 214 $cm^2V^{-1}s^{-1}$ and high on/off ratios of 10^7 at room temperature [36].

In MOSFETs, the charge carriers surmount the potential barriers between the source and channel by thermal injections and thus the theoretical minimum of subthreshold swing (SS) is 60 mV/dec. In contrast, in a tunnel field-effect transistor (TFET) the charge carriers inject into the channel by interband tunneling which is turned on and off abruptly by gate biasing over the channel with steep band bendings [37]. As a consequence, as Figure 1.7 (b) [5] illustrates, the SS of TFETs can reach below the theoretical minimum of SS in normal FETs and thus TFETs can maintain the same performance and achieve the required same on/off ratios with a smaller voltage swing compared to the normal FETs. Thus, TFETs are more energy efficient. Recently, a vertical heterostructure TEFT, consisting of highly doped germanium as the source and bilayer MoS_2 as the channel, exhibited an average of 31 mV/dec at room temperature [38]. The absence of surface dangling bonds in 2D materials and the reduced surface states make 2D materials candidate materials for TEFTs, which needs further exploration.

Although TMD FETs exhibit encouraging results, there remain many challenges in the applications of TMD FETs. One of the major challenges is the high contact resistance, which results in reduced drain current [4]. Typical contact resistances of 10 kΩ•μm and larger at the source and drain were reported in MoS_2 FETs [29, 34, 39], arising from the atomically thin body of 2D TMDs. Au contacts were reported to make ohmic contacts to MoS_2, showing linear relations between current and voltage [3, 35]. Theoretically, Au forms a Schottky barrier with n-type MoS_2 due to higher work function of Au. However, the author argued that the atomically thin body of 2D MoS_2 enables a narrow width of Schottky barrier and thus results in carrier tunneling through the barrier and relatively low resistances [34]. However, the ohmic contact from Au is not always formed to 2D TMDs, strongly depending on the material quality of 2D TMDs, Au deposition conditions and device fabrication processes, in our devices that will be discussed in the following chapters. Scandium contacts were studied to effectively reduce the contact resistance in 10nm thick exfoliated MoS_2 flakes and obtain a high effective mobility of 700 $cm^2V^{-1}s^{-1}$ at room temperature [34]. Graphene, as a semi-metallic 2D material, was shown to be a good contact material for low contact resistances in MoS_2 FETs [32, 40]. Reduction of contact resistances has become one of the important topics in 2D materials and constant efforts and innovative methods, including phase engineering [39] and doping [41], have been implemented to eliminate large resistances and realize high-performance FETs.

Optoelectronic Devices

Monolayer TMDs are appealing for optoelectronic devices due to their direct bandgaps in visible light spectrum and strong PL spectrum. Monolayer MoS_2 based photodetectors have been investigated extensively [29, 42, 43]. In particular, spatial/temporal photocurrents and electronic transport were studied in monolayer MoS_2 grown by chemical vapor deposition (CVD) with the structure of phototransistor and Hall bar devices [29]. The maximum photocurrent occurs when the laser spot is close to the contact and is tunable by

the applied drain voltage due to the modulation of the local electric field at the Schottky barrier. And the maximum photocurrent at the drain contact is much larger than that at the source contact because of higher Schottky barrier at the drain contacts extracted from the current-voltage relations at various temperatures. The extracted photoresponsivity of the monolayer MoS2 photodetector is 3.07mA/W. This relatively low photoresponsivity is mainly ascribed to the low light absorption of monolayer MoS_2.

Other than photodetectors, explorations of photovoltaics based on 2D TMDs have been made due to their direct bandgaps in tunable range (1 eV-2 eV) and relatively large earth abundance [44]. Monolayer MoS_2 was reported to form type II heterojunction with p-type silicon and achieved a remarkable power conversion efficiency > 5% [45]. The other types of materials and heterojunctions, such as WSe_2/MoS_2, were also studied for the photovoltaic effect [46] and one of the challenges is the low light absorption due to the atomically thin body. However, 2D materials exhibit promising applications in thin film and flexible photovoltaics and need further investigations.

Another appealing application of 2D TMDs is flexible light-emitting diodes (LEDs) due to their direct bandgaps in monolayer. Electroluminescence (EL) was detected in monolayer MoS_2 on glass substrates with Schottky junctions [47]. A heterojunction of monolayer MoS_2 and p-type Si was also observed to have light emissions [48]. By utilizing BN as bottom dielectrics lateral p-n diodes in monolayer WSe_2 emitted brighter electroluminescence due to more effective carriers injection than MoS_2 [49]. However, novel device structures and better surface engineering are needed to improve the low quantum efficiency for more efficient light emission.

Flexible Electronics

The pursuit of future flexible and transparent electronics has motivated the research community to explore candidate materials over a long time. The conventional Si can be thinned down for UTB applications [50, 51], but the

carrier scattering and brittle nature pose limitations for current Si technology in the practical flexible applications. Organic semiconductors are also promising for flexible large area devices, but their relatively poor physical and electrical properties limit their performance and applications [52]. 2D materials have attracted considerable attention as an ideal candidate material due to their excellent mechanical properties [53, 54], large scale growth by CVD [55] and easy transfer to varieties of substrates [56], atomic and transparent body, and high integration of diverse 2D materials with various functionalities [7]. Thin film MoS_2 transistors have been fabricated on polyimede substrate, revealing a high on/off ratio of 10^5 and high mobility of 12.5 $cm^2V^{-1}s^{-1}$, and maintaining a high performance even with significant bending [57]. Graphene was also fabricated on flexible substrate with gate dielectric of HfO_2 and metal electrodes and gates, and achieved gigahertz frequency power gain with strains up to 1.5% [58]. The advancement in 2D materials research has accelerated the development of flexible electronics and more research reports have demonstrated encouraging results [59-61]. However, the field is still facing serious challenges that need to be addressed for the commercialization of 2D materials based flexible electronics, such as feasible fabrication processes at low cost, development of complementary transistor technology, etc. [11]. Sustainable research effort will find solutions and transform the 2D materials into practical high-performance flexible electronics in the foreseeable future.

1.4 Challenges and Research Objective

The unique and remarkable properties of 2D materials make them promising candidates for novel electronic and optoelectronic devices with broad applications. However, the investigations of 2D TMDs are still in early stages with many challenges. For example, the contact resistance is still a severe issue limiting the device performance. And a large-scale materials growth method is indispensable for high-quality mass production. Moreover, a feasible processing of 2D TMDs compatible with the conventional semiconductor processing is essential to produce commercialized products at low cost.

In this thesis, the research objective is mainly to study the electrical and optical properties of 2D materials and electronic devices based on these materials. In chapter 2, the processes of materials preparation, materials characterization and devices nanofabrication will be discussed in detail. In chapter 3, the investigation of MoS_2 and WS_2 heterostructures will be discussed. In chapter 4, the study of polarized Raman scattering and anisotropic electronic transport of a new 2D material, germanium selenide (GeSe), will be presented.

1.5 Figures

a

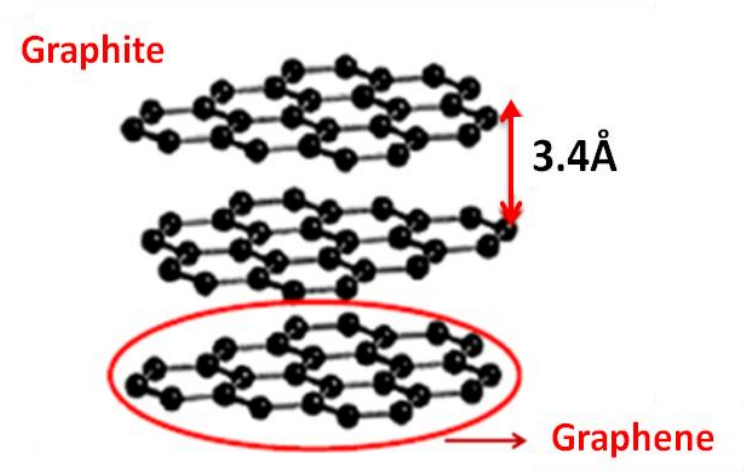

b

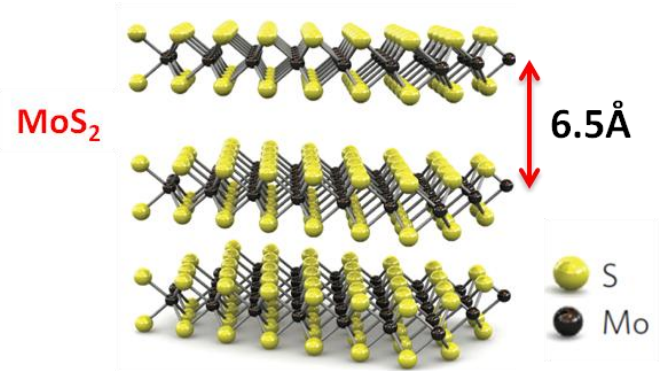

Figure 1.1 The atomic structures of (a) graphene [2] and (b) MoS_2 [3].

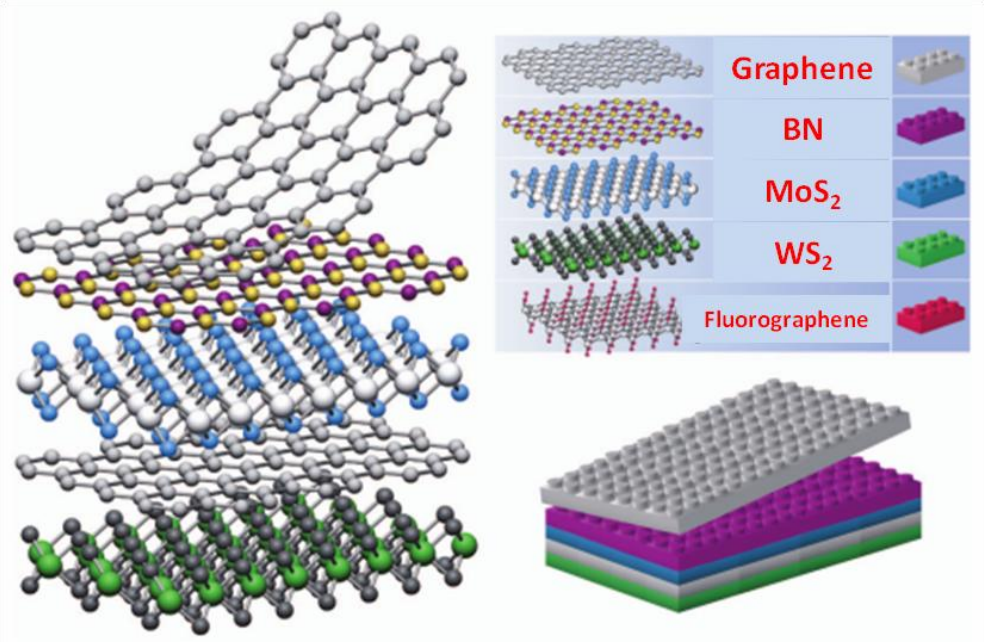

Figure 1.2 Forming heterostructures with various 2D materials in random orders [6].

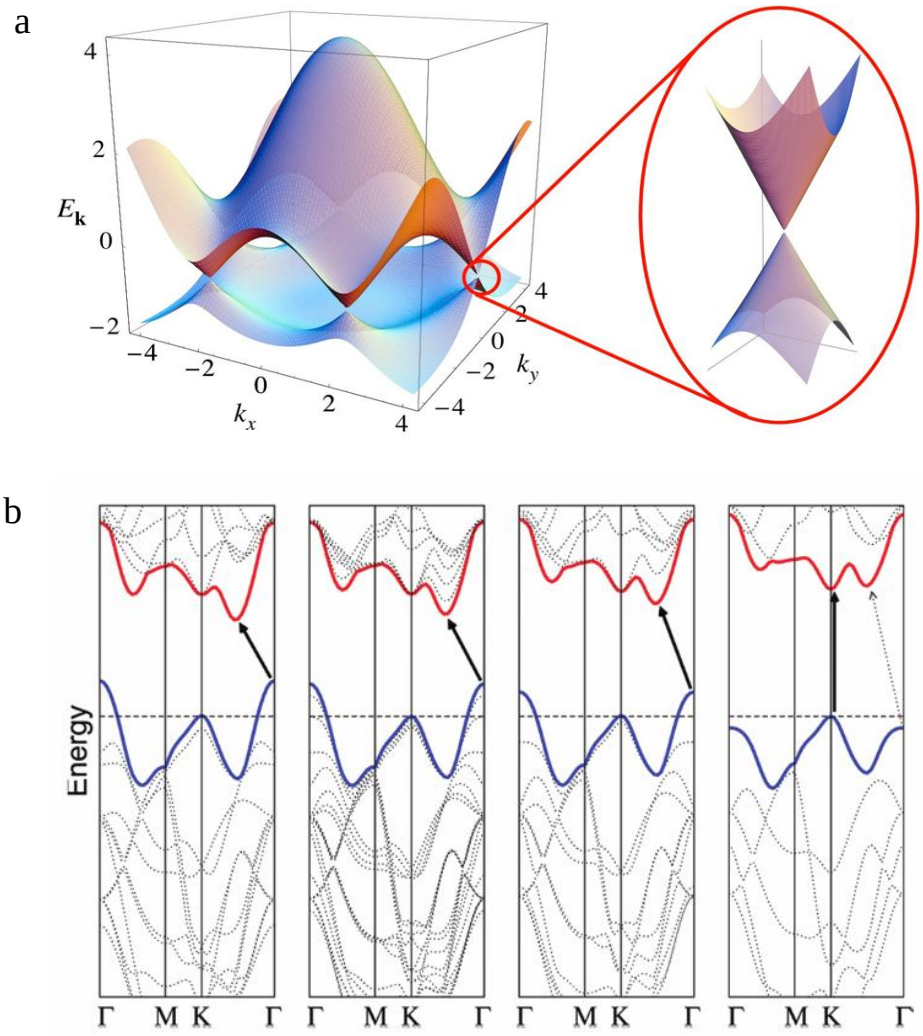

Figure 1.3 Energy dispersion in (a) graphene [15] and (b) MoS_2 bulk, quadrilayer, bilayer and monolayer from left to right [26].

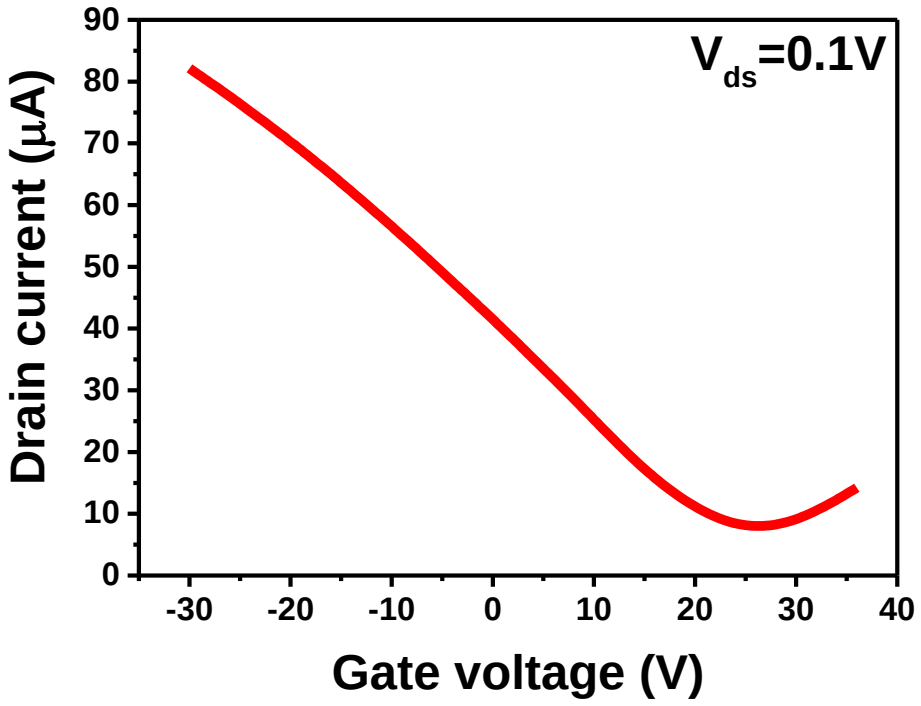

Figure 1.4 The transfer characteristics of graphene transistor, showing high off-state current.

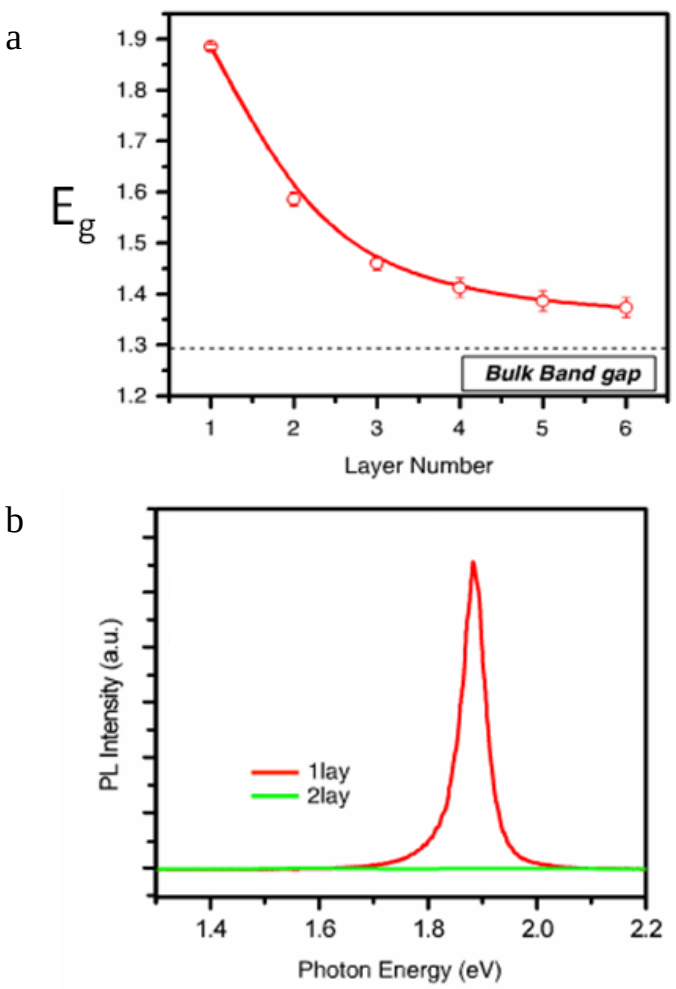

Figure 1.5 (a) The evolution of bandgap of MoS_2 in different thicknesses. (b) Photoluminescence spectra of monolayer and bilayer MoS_2. [27]

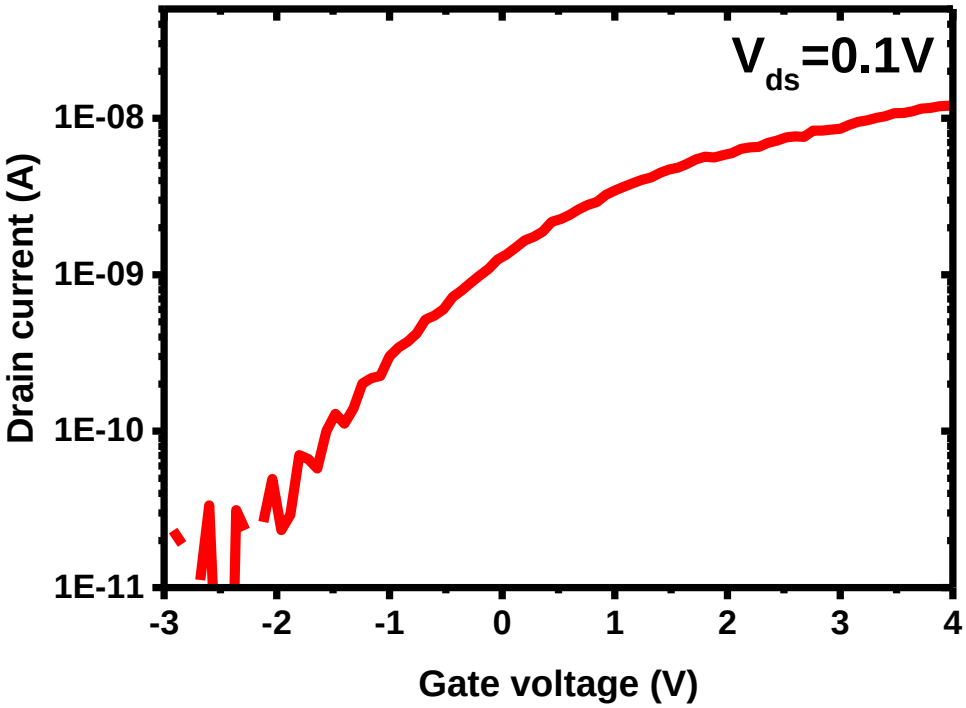

Figure 1.6 The transfer characteristics of monolayer MoS_2 transistor, showing low off-state current.

a

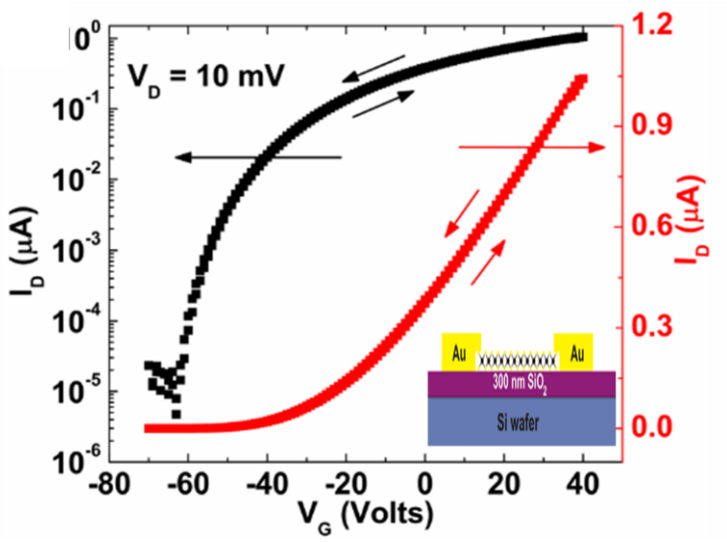

b

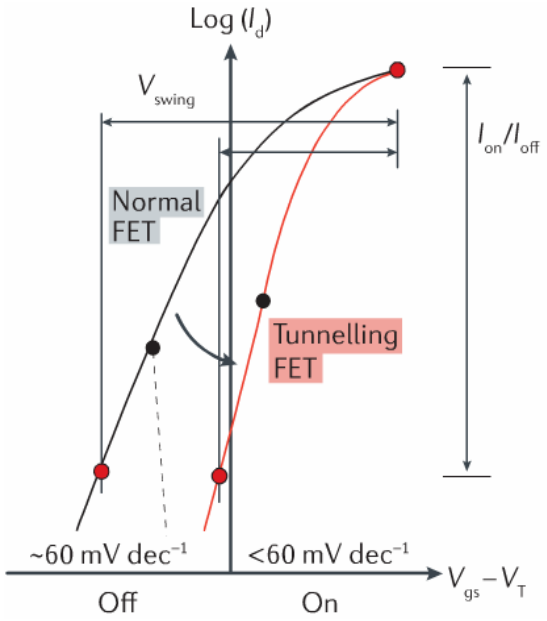

Figure 1.7 (a) Transfer characteristics of single-layer MoS_2 FET. The inset shows the device structures. [35] (b) Transfer characteristics of a TFET and a normal FET in which the TFET shows a SS smaller than 60 mV/dec while keeping the same on/off ratio as the normal FET. [5]

Chapter 2 Experimental Details

2.1 Introduction

Unlike the devices based on conventional 3D or bulk semiconductor materials, electronic devices based on 2D materials cannot be processed using the conventional semiconductor processing methods due to their unique nature, such as their atomically thin body, high sensitivity arising from their high surface-volume ratio, etc. For example, Si is usually treated by plasma etching after the step of photolithography in order to remove the photoresist residual and clean the Si surface for good device performance. However, if plasma etching is used to treat and clean the surface of 2D materials, they will be damaged severely or etched away completely. So far, it is impossible to precisely control the process of plasma etching using the conventional semiconductor processing facilities with reasonable parameters to clean the surface of 2D materials. Thus, alternative and feasible processing methods must be explored specifically for the 2D materials in order to fabricate high-performance devices and study their fundamental properties.

In this chapter, a complete process, including 2D materials preparation/ characterization and device fabrication/characterization, is developed and discussed, which lays foundation for the research of 2D materials based electronic and optoelectronic devices. The devices based on MoS_2 and WS_2 heterostructures in chapter 3 and transistors based on GeSe in chapter 4 are investigated using this process.

2.2 Material Preparation

2.2.1 Mechanical Exfoliation

In 2001, single-layer graphene was produced by mechanical exfoliation from bulk graphite for the first time using Scotch tape [14] as shown in Figure 2.1(a). Since then, mechanical exfoliation has been used as a primary method to

produce atomically thin 2D materials from bulk materials. As the name implies, mechanical exfoliation is defined as a technique that uses an external force, such as micromechanical cleavage using the Scotch tape, to overcome the weak interlayer van der Waals force and peel atomic layers apart [62], and then achieve atomically thin materials as illustrated in Figure 1.1.

The general procedure of mechanical exfoliation using Scotch tape is divided into two parts. The first step is to thin down the bulk materials by putting them onto the Scotch tape and peeling off repeatedly until the thick bulk materials are thinned down to some degree as shown in Figure 2.1 (b). The second step is to transfer the exfoliated flakes on the tape to the surface of a substrate by sticking the tape on the substrate. A few finished samples are shown in Figure 2.2 and 2.4. After the transferring of the flakes, optical inspection is used to identify the suitable flakes for the subsequent material characterization and device fabrication.

As can be seen in Figure 2.2, there are built-in alignment marks in the form of numbers and squares on the substrate, circled in red together with the material flakes. Since the flakes in various shapes are transferred and then distributed on the surface of substrates in a random order, the alignment marks are needed to record the location of the desirable flakes for the subsequent processing. The period of the alignment mark arrays is 76 μm and they are repeated over the entire surface of the substrates. The numbers indicate the row and column of the alignment marks respectively. For example, the numbers of 30 and 29 in Figure 2.2 surrounded by four square marks indicate the column number is 30 and row number is 29.

Considering the importance of the alignment marks on the substrates for identifying flakes, preparation of substrates with these built-in alignment marks is a prerequisite step before the micromechanical cleavage and subsequent processing. Figure 2.3 demonstrates a process flow of alignment marks fabrication on a Si wafer utilizing the dry etching process. It starts with a Si

wafer with a layer of SiO_2 as shown in Figure 2.3 (a). Using photolithography, the patterns on the photomask are transferred to the photoresist (PR) as shown in Figure 2.3 (b). And then the Si wafer with the patterned PR is transferred into the chamber of a Freon reactive ion etcher which produces high energy and high density reactive plasma with an etchant of CF_4 gas. The CF_4 plasma does not have a good selectivity and is able to etch the PR, SiO_2 and Si simultaneously, and the etching rate ratio for PR, SiO_2 and Si is about 2:1:2. Thus, 1.4 μm thick PR is good enough to function as the protection layer and enable the plasma to etch a well into the Si wafer with steep side-walls to a depth of 0.5 μm -1.0 μm, as shown in Figure 2.3 (c). The steep side-walls that are produced by the dry etching are critical to an accurate alignment in the subsequent E-beam writing step. After desirable etched thickness in Si is achieved, the next step is to remove the remaining PR with acetone and SiO_2 with diluted hydrofluoric acid solution. The bare Si wafer is shown in Figure 2.3 (d) after it is complete. In order to use the Si body as a bottom gate for electronic devices, a bottom gate dielectric layer is needed on the top of the Si wafer. Thus, a layer of high quality SiO_2 is grown by dry oxidation on the top of Si body, as shown in Figure 2.3 (e). A certain SiO_2 thickness (e.g., 90 nm, 280 nm) is required to take advantage of the color contrast arising from the effect of light interference on SiO_2 to recognize the exfoliated material flakes using the optical microscopy [63]. Up to this point, the substrate with built-in alignment marks has been completed, and the top view of the wafer is shown in Figure 2.3 (f).

Once the substrate with built-in alignment marks is ready, the mechanical exfoliation using Scotch tape can be used to obtain some 2D materials sheets. Although this method is widely used to obtain thin and large graphene sheets, it has limitations of obtaining thin and large sheets of other 2D materials, such as MoS_2 and GeSe. With the Scotch tape, too much tape residual usually is left over on the substrate, which inevitably results in problems in the process of device fabrication and degrades the device performance. The solution to this problem is to use an alternative tape, called blue tape as seen in Figure 2.1 (c), which comes with less tape residual while maintaining the necessarily large

adhesion force to peel the layered materials apart. Moreover, another problem is low yield. For this problem, high power O_2 plasma is used to pretreat the surface of the substrate before transfer. The function of high power O_2 plasma is believed to make a perfectly clean SiO_2 surface and probably induce extra electrostatic charges on the surface, which effectively promotes the adhesion between materials and SiO_2 surface and thus increases the yield in exfoliation. Another common problem is that the exfoliated flakes are small in thickness and size. In order to obtain desirably thin and large sheets, one needs an improved hands-on skill that requires longer time for pulling tapes off the substrate extremely slowly in a direction that is almost parallel to the substrate. With these significant improvements, the problems are resolved, and thin and large enough materials sheets are obtained. As seen in Figure 2.4 (a) a graphene sheet is up to 30 μm large and Figure 2.4 (b) shows a GeSe sheet up to 40 μm large in a thickness of about tens of nanometers.

In addition to the micromechanical cleavage using tape, there are other mechanical exfoliation techniques reported, such as sonication assisted liquid-phase method [64], ball milling method that utilizes shear force for lateral exfoliation [65], fluid dynamics method that utilizes lifting and slippage on the tube wall [66], etc. All the techniques are developed to generate a normal force or shear force to defeat the weak van der Waals force, and they all have their own advantages and disadvantages as discussed in reference [62]. However, the various mechanical exfoliation techniques need further improvements, and novel methods need to be developed for higher efficiency and large-scale production.

2.2.2 CVD Growth

Due to the limitations in mechanical exfoliation techniques, a more feasible and mature method is imperative to produce high-quality and large-scale 2D materials not only for the purpose of research but also for future practical applications. In 2009, Li *et al.* [67] reported a breakthrough in the growth of single layer graphene by CVD. In this work, a large-area single layer graphene

was achieved with methane and hydrogen as gas sources and copper foil as substrates that were removed later by chemical etching for graphene films transfer. This work opened up the large-scale synthesis of graphene by CVD with precise control of layers in single crystal on various substrates [68-70].

In 2012, Lee *et al*. [55] reported for the first time that large-area single layer MoS_2 was synthesized successfully by CVD on SiO_2/Si substrates with MoO_3 and sulfur powders as precursors and perylene-3,4,9,10-tetracarboxylic acid tetrapotassium salt (PTAS) as growth promoters, and figured out that the growth was very sensitive to the substrate treatment and growth conditions in CVD furnace. Similarly, CVD has been used to synthesize other TMDs. The CVD growth of monolayer WS_2 in large single crystal domains was reported by precise control of growth temperature, time and amount of precursors and the grown monolayer WS_2 was up to several hundred microns [71, 72]. Moreover, TMDs-based heterostructures were successfully synthesized as well. Vertical and lateral monolayer-WS_2/monolayer-MoS_2 heterostructures of high quality were achieved by CVD using a one-step vapor phase growth process via growth temperature control respectively for MoS_2 and WS_2, and a strong interlayer excionic peak was observed at 1.42 eV by PL spectroscopy that arises from the type II band alignment and atomically sharp interfaces in the WS_2/MoS_2 heterostructures [73]. Various other heterostructures, such as $WSe_2/MoSe_2$, WSe_2/MoS_2, etc., were also reported [74, 75] so that novel electronics and optoelectronics are possibly investigated by taking full advantage of the unique properties of TMDs-based heterostructures that will be discussed in chapter 4.

In addition to the semi-metallic and semiconducting 2D materials, the growth of insulating 2D dielectric material, boron nitride (BN), was also realized by CVD, which is more challenging. Borazine vapor in nitrogen gas flow was used to grow BN in tens of nanometers thickness on polycrytalline nickel substrate [76]. Ammonia borane was also used as precursor in Ar/hydrogen gas flow to achieve high-quality BN thin films of large size [77].

So far, the capability of CVD for growth of diverse 2D materials has been demonstrated. However, substantial efforts are needed to develop better synthesis methods of 2D materials of higher quality with fewer defects, in larger scale and with low cost for future practical applications.

The MoS_2 and WS_2/MoS_2 heterostructure thin films studied in this thesis were synthesized with a CVD setup and recipe similar to that used in reference [55], as illustrated in Figure 2.5 (a). The CVD furnace is divided into two zones, where sulfur powder is located at the low temperature zone (200 ℃) while MoO_3 powder is located at the high temperature zone (750 ℃). The SiO_2/Si substrate is placed close to or above the MoO_3 precursor. Prior to putting the precursors and substrate into the furnace, a diluted PTAS solution is spun on the surface of the substrate which is then transferred to the furnace after it dries. During the synthesis, high purity Ar is flowing as carrier gas that carries the vapor sources of S and MoO_3 to the substrate, and then MoO_3 is reduced chemically by S and thus MoS_2 films are produced. One crucial procedure prior to growth is to use piranha solution to treat the SiO_2/Si substrate, which is believed to make the surface highly hydrophilic and keep PTAS on the surface uniformly during spinning and drying. Since the grown MoS_2 films are very sensitive to the growth conditions, optimization of growth parameters (e.g, zone temperatures, Ar flow rate, growth time, etc.) eventually results in monolayer MoS_2 films up to 50 μm wide as shown in Figure 2.5 (b) and even continuous monolayer MoS_2 films as shown in Figure 2.5 (c).

2.3 Materials Characterization

After the 2D materials are grown successfully, several materials characterization techniques are used to characterize the materials and examine surface morphology, thickness and quality.

The most straightforward technique is optical microscopy. As discussed earlier, it is able to recognize the thin 2D materials films by color contrast on SiO_2 arising from the effect of light interference [63]. Thus, optical microscopy is

usually first used to inspect the thin films on the substrate and get a rough idea of the films morphology and size before more accurate and higher resolution techniques are conducted. Typical images acquired by optical microscopy are shown in Figure 2.1, 2.4, 2.5 (b) and (c).

The film morphology of the samples in this work is examined using a Hitachi S4800 scanning electron microscope (SEM) or an Asylum Research MFP-3D atomic force microscope (AFM) with Cr/Pt tips from BudgetSensors (TAP300AL). AFM is able to generate images at extremely high resolution and examine features at the atomic level, which makes AFM a perfect technique to characterize 2D materials. Figure 2.6 shows an AFM image of surface morphology of MoS_2 films, which can be used to measure the exact thickness of the MoS_2 films. Moreover, this high-resolution AFM image can also give the thickness variation and the distribution of contaminants across the entire surface.

More importantly, Raman and PL spectroscopy are quick techniques that are widely used to examine the exact number of layers of 2D materials. Photoluminescence is a process of photon absorption and radiation where the materials absorb photons from a light source. The energy of the absorbed photons is greater than the bandgap, and then it emits photons with the energy not greater than the absorbed photons. In direct bandgap semiconductors, the absorbed photons excite electrons and holes, and then the excited electrons and holes are able to directly recombine and radiate as photons. However, in indirect bandgap semiconductors, the radiative recombination of the excited electrons and holes requires the participation of phonons with their relatively large momentum to conserve momentum during the process; thus, a process that needs the participation of three particles (i.e. electron, holes and phonons) is much less likely than what occurs in direct bandgap semiconductors with the participation of only two particles. Therefore, PL in direct bandgap semiconductors is much more efficient than in indirect bandgap semiconductors.

Thus, this strong and unique feature enables a quick technique with PL spectrum to identify the monolayer of MoS_2 with a direct bandgap, which is used extensively to characterize the material and differentiate the monolayer from other thicknesses of MoS_2 [26]. As Figure 1.6 (a) illustrates, a strong PL peak is only observed in monolayer 2D TMDs, which can be used to distinguish monolayer from non-monolayer 2D TMDs.

More accurately, Raman spectroscopy can also be used to determine the number of layers of 2D TMDs. Figure 2.7 (a) diagrams the Raman and Rayleigh scattering processes [78]. The mechanism of Raman scattering involves the interactions between incident light with a single frequency (e.g., 532 nm laser) and the molecules. It results in polarization of the electron cloud around the nuclei and creates so-called "virtual states" temporarily, as shown in Figure 2.7 (a), and the scattered radiation from the molecules is detected to tell the difference from the incident radiation. The difference is defined as Raman shift and expressed as the following formula: $\Delta\omega = \frac{1}{\lambda 0} - \frac{1}{\lambda 1}$, where $\Delta\omega$ is the Raman shift, λ_0 is the wavelength of incident excitation laser, and λ_1 is the wavelength of scattered radiation.

As Figure 2.7 (a) (1) illustrates, the Rayleigh scattering is an elastic scattering process that does not induce any energy change in photons and light goes back to the original state, since it only causes polarization of electron cloud without nuclear motion. In contrast, as Figure 2.7 (a) (2) and (3) illustrate, the Raman scattering process is an inelastic scattering process that causes nuclear motion and there is energy exchange between photon and molecule. One kind of Raman scattering is Stokes scattering, which involves an energy transfer from incident photon to the molecule. If the energy is transferred from molecule to scattered photon, this Raman scattering process is anti-Stokes scattering. Compared to Rayleigh scattering, the probability of Raman scattering is very small.

Since the Raman spectrum provides vibrational information of the phonon structure specific to molecules which have unique Raman peaks in Raman

spectra, it is used as a fingerprint to identify the molecule and an effective and quick technique to differentiate one from others. Figure 2.7 (b) exhibits the Raman spectra of MoS_2 for various thicknesses from monolayer to bulk with a 532 nm laser light [79]. Two Raman peaks are observed in various thicknesses of MoS_2. One corresponds to in-plane E^1_{2g} mode, located at 384 cm^{-1} and the other out-plane A_{1g} mode, located at 408 cm^{-1}. And the exact positions of E^1_{2g} mode and A_{1g} mode are functions of MoS_2 film thickness. As the MoS_2 film thickness increases, E^1_{2g} mode decreases but A_{1g} mode shifts in an opposite direction, which originates from the effective restoring forces and long-range Coulomb interactions [80]. The noticeable shifts of E^1_{2g} mode and A_{1g} mode make the Raman spectra an excellent indicator of thickness in MoS_2 film, which also applies to other 2D TMDs, such as WS_2, $MoSe_2$, etc.

The above characterization techniques are frequently used to characterize the 2D materials studied in this thesis. Chapters 3 and 4 will discuss specifically the characterization of WS_2/MoS_2 heterostructures and GeSe. In addition to AFM, PL and Raman spectroscopy, many other techniques (e.g., TEM, second harmonic generation and etc.) are also used to characterize the 2D materials, which will not be discussed in this thesis.

2.4 Device Fabrication

After a series of materials characterizations, high-quality materials are used to fabricate electronic and optoelectronic devices by a nanofabrication process that is developed with the conventional semiconductor fabrication facilities and discussed as follows.

Figure 2.8 depicts the process flow of 2D-material based device fabrication. The complete fabrication process involves several runs of lithography, either photolithography or E-beam lithography. Although these two types of lithography have some differences in the specific photoresists, developers and facilities, they basically have the same process steps in the flow. E-beam lithography will be taken as an example to demonstrate this complete flow. The

process starts with 2D material thin films on SiO_2/Si substrate as shown in Figure 2.8 (a), and the 2D material thin films are obtained from either the mechanical exfoliation or the CVD growth. The first step of E-beam lithography is to spin a layer of 200 nm thick PMMA (e.g., 950K A4). Then the sample is written by electron beam with a dose of $220\,\mu C/cm^2$. After development of the sample in the solution of 1:3 MIBK: IPA for 120 seconds, the designed pattern will be formed in the PMMA on the sample. Figure 2.8 (b) depicts the patterned PMMA with 2D material thin films which is partially covered by the layer of PMMA coating and partially exposed for next step processing. As depicted in Figure 2.8 (c), a step of metallization is done and metal contact is made to the 2D materials where they are not covered by the PMMA coating. Usually, this metal layer consists of 5-10 nm thick Ti and 35nm or thicker Au and the total thickness should not be larger than one third of the PMMA thickness so that the subsequent lift-off is easy to implement for a well-designed device configuration. After metal lift-off in acetone, a bottom-gated MOSFET device based 2D materials is completed as depicted in Figure 2.8 (d). At this point, an extra run of E-beam lithography patterning and oxygen plasma etching is usually needed to cut the 2D material thin films into a rectangular shape with designed width and length as the device channel, which is not demonstrated in the process flow in Figure 2.8.

In some cases where the bottom dielectric does not function well or a better gate control is needed to form a dual-gate device with a top gate, the fabrication process needs to continue for the addition of a top gate. As depicted in Figure 2.8 (e), a layer of top dielectric about 20 nm thick is deposited on the top of the bottom-gated device. Based on the facility feasibility in the cleanroom on campus, this dielectric could be ALD-deposited HfO_2 or PECVD-deposited silicon nitride in high quality. With another run of E-beam lithography patterning, metallization and lift-off, the top gate metal applies to the device and a complete device is configured as Figure 2.8 (f). Up to this point, the device fabrication process is completed and the device is ready for characterizations and further analysis.

2.5 Device Characterization and Problems

For the electronic devices, one of the most important characterization tools is probe station as shown in Figure 2.9. This probe station system is equipped with six probing arms and able to conduct many functions and a variety of electrical measurements at various temperatures from 4K to 400K, such as current-voltage measurement, capacitance-voltage measurement, Hall-effect measurement, etc. All the data of electrical measurements discussed in this thesis are acquired by this type of probe station.

In terms of the device size studied in this thesis, the long channel MOSFET equation for calculating drain current is modeled as [81]:

$$I_D = \mu Ci\frac{W}{L}[(V_{GS} - V_T)V_{DS} - \frac{1}{2}V_{DS}^2],$$

where I_D is the drain current, μ is the carrier mobility, Ci is the gate dielectric capacitance per unit area, W and L are the channel width and length, V_T is the threshold voltage, V_{GS} and V_{DS} are the gate voltage and the drain voltage respectively with respect to the grounded source. The field-effect mobility in low field for small V_{DS} can be extracted from the above expression as:

$$\mu = L/(WCiV_{DS})\bullet(dI_D/dV_{GS}).$$

The subthreshold swing (SS) is defined as:

$$SS = [d(\log_{10}I_D)/(dV_{GS})]^{-1},$$

which represents how much change in gate voltage would result in a decade of change in drain current. According to the definition, a smaller SS is favored, which denotes a better gate control over the channel. For the conventional MOSFETs with thermal injections, the theoretical minimum of subthreshold swing (SS) is 60 mV/dec.

Figure 1.4 demonstrates the transfer characteristic of the bottom-gated graphene transistor. Given that L/W is 3, Ci = $1.3*10^{-8}$ F/cm^2 is the gate oxide capacitance

per unit area for 270 nm thick SiO_2 (ε_r = 3.9), the extracted field-effect mobility is around 4300 $cm^2/(V•s)$.

Similarly, Figure 1.5 demonstrates the transfer characteristic of the top-gated monolayer MoS_2 transistor. Given that L/W ≈ 3.5, Ci = $8.6*10^{-8}$ F/cm^2 is the gate dielectric capacitance per unit area for 20 nm thick HfO_2 (ε_r = 19.5), the extracted field-effect mobility is even smaller than 1 $cm^2/(V•s)$. The ON/OFF ratio is about 10^3 and the subthreshold swing (SS) is astonishingly larger than 500 mV/dec.

One key problem that severely degrades the device performance of TMD transistors is the high contact resistance. Figure 2.10 (a) illustrates a zoomed-in contact with a layer of PMMA residual between metal and the 2D materials. If the layer of PMMA residual is thick enough, it will result in an insulating contact and malfunctioning device. Even if the layer of PMMA residual is thin, it will result in a large contact resistance and thus degrade the device performance significantly. One obvious phenomenon from the large contact resistance is low drain current in the device, which is often at the level of nanoampere (nA). Therefore, it is important to remove the PMMA residual as much as possible. Usually, the silicon is cleaned and the photoresist is removed by plasma after the photolithography processing. However, if plasma etching is used to treat and clean the surface of 2D materials, 2D materials will be damaged severely or etched away completely due to the atomically thin body of 2D materials. It is very difficult to precisely control the process of plasma etching using the conventional semiconductor processing facilities with reasonable parameters to clean the surface of 2D materials. Alternatively, the solution is to adjust the parameters in the E-beam lithography processing, such as increased dose to 250-300 $\mu C/cm^2$ and extended development time to 150 seconds or longer until the distortion in patterns appears. As such, the PMMA residual could be removed more thoroughly but at the cost of lowering the resolution of the E-beam lithography processing.

In addition to the appearance of PMMA residual at the contacts between metal and the 2D materials, PMMA residual is also left over on the surface of 2D materials due to the acetone treatment which cannot remove the PMMA fully [82, 83]. The carrier transport is significantly affected by the PMMA residual which brings extrinsic scattering onto the surface of 2D materials and acts as the scattering center to reduce the mobility remarkably. Moreover, the subsequent top-gate dielectric deposition would make the PMMA residual exist at the interface between 2D materials and gate dielectric, and thus the interface states would greatly increase, which can result in a shift of threshold voltage. Actually, removing PMMA fully from the surface of the 2D materials is challenging. However, some approaches can be used to reduce the impact of the PMMA residual to some extent. Soaking the samples in warm acetone (e.g., 50 ℃) for a long time (e.g., 24 hours) is believed to be helpful. More importantly, device annealing in forming gas has been proven successful in removing PMMA residual from graphene [83]. With the established processes for the device nanofabrication, a similar annealing step is developed and added to the process flow. The device annealing is performed in the forming gas Ar/H_2 (4:1) at 200 ℃ for 2 hours before the implementation of top-gate dielectric deposition.

Another problem that arises from the E-beam lithography processing is shown in Figure 2.10 (b). The disconnected metal-lines circled in red result in an open circuit in the device. The fine lines in the metal connections are mainly from the stitching error due to the E-beam lithography writing system. Instead, the E-beam lithography writing is executed by patterning one device completely in one writing field and avoiding any stitching in the writing filed around the effective device area on the substrates.

Another common problem in devices is large gate leakage current. Figure 2.11 (a) depicts large gate leakage current over 10 nA and higher. Some devices even have a gate leakage current over 1 μA. Generally speaking, a well-designed device with high-quality gate dielectric has a reasonable gate leakage current at the level of picoampere (pA). Thus, the large leakage current is mainly

attributed to the gate dielectric in low quality and the relatively thinner gate dielectric in the overlap region between gate and drain/source as the zoomed-in inset in Figure 2.11 (b) demonstrates. To solve the problem of large gate leakage current, a high-quality and relatively thick gate dielectric can be produced by a better deposition system, such as the ALD-deposited HfO_2 or PECVD-deposited silicon nitride. Moreover, the thickness variation in gate dielectric exacerbates the problem from the thinner gate dielectric in the overlap region. The solution is to add a seed layer of Al, several nanometers thick, which is then oxidized as aluminum oxide. This is followed by the gate dielectric deposition. This improvement could result in a more uniform gate dielectric layer with less variation in the thickness.

2.6 Summary

By continuous troubleshooting, various problems arising from the materials and process flow are recognized with the device characterizations and then corresponding solutions are explored and executed effectively. Eventually, a complete process flow, ranging from materials preparation to device fabrication, has been successfully developed and established.

As a key part of this thesis, this chapter discusses the entire process flow in detail. Chapters 3 and 4 are based on this standard process flow to fabricate devices and investigate the WS_2/MoS_2 heterostructures and GeSe, respectively.

2.7 Figures

a

b

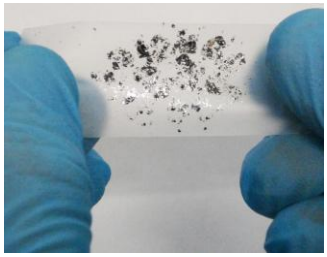

c

Figure 2.1 (a) Scotch tape used for mechanical exfoliation. (b) Material flakes on scotch tape. (c) Blue tape for improved mechanical exfoliation to reduce the tape residual

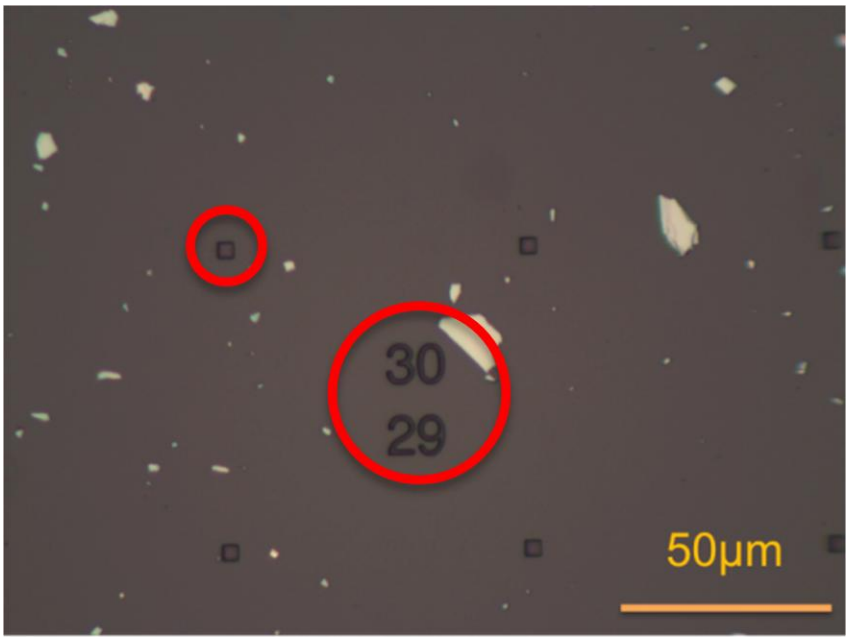

Figure 2.2 An optical image of a Si wafer with alignment marks (circled in red) and randomly distributed material flakes in top view.

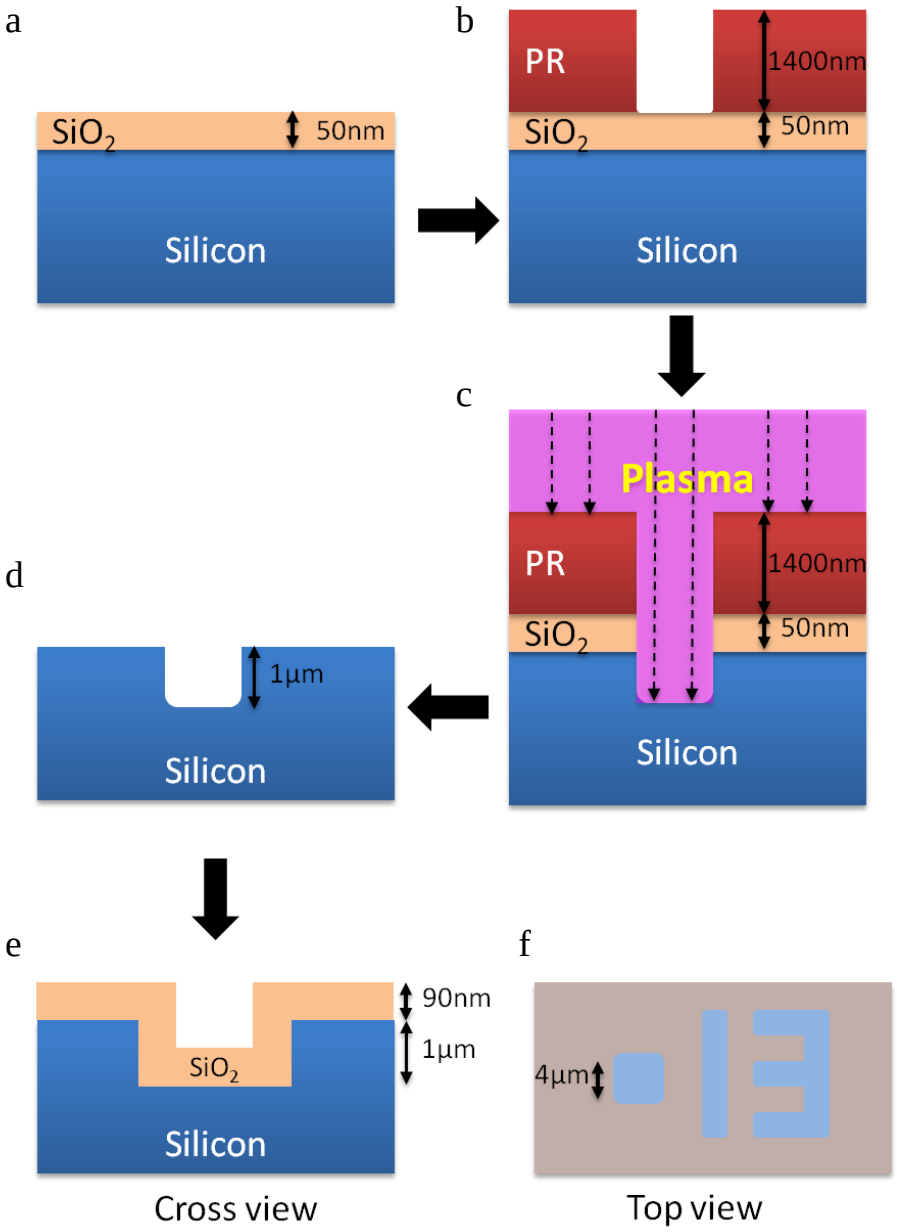

Figure 2.3 The process flow of alignment marks fabrication on a Si wafer.

a

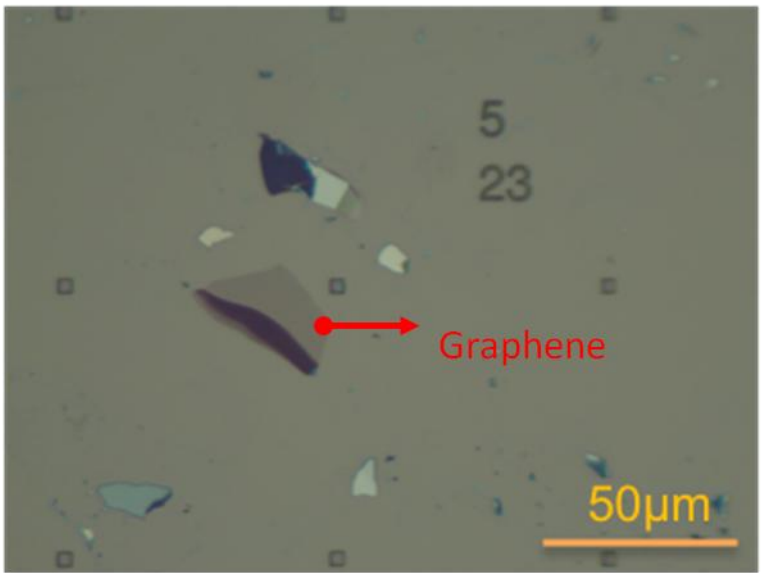

b

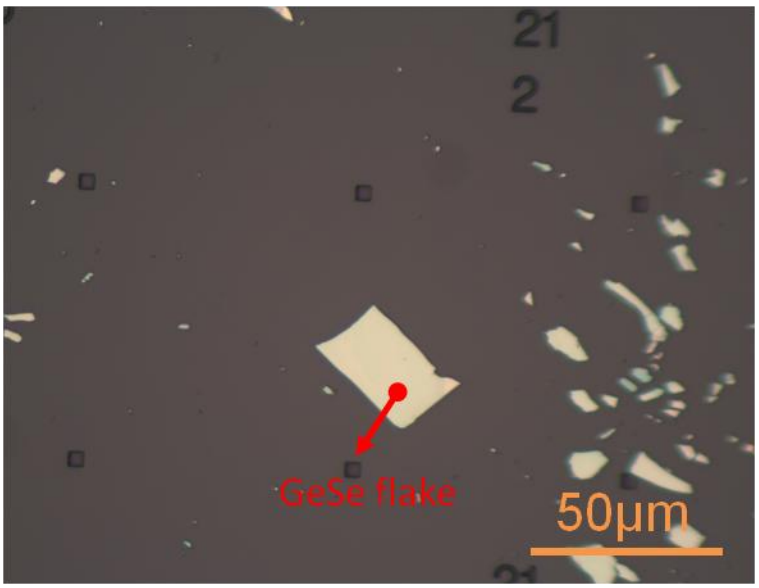

Figure 2.4 Optical images of (a) graphene sheet and (b) thin GeSe sheet on SiO_2/Si substrates obtained by the improved mechanical exfoliation.

a

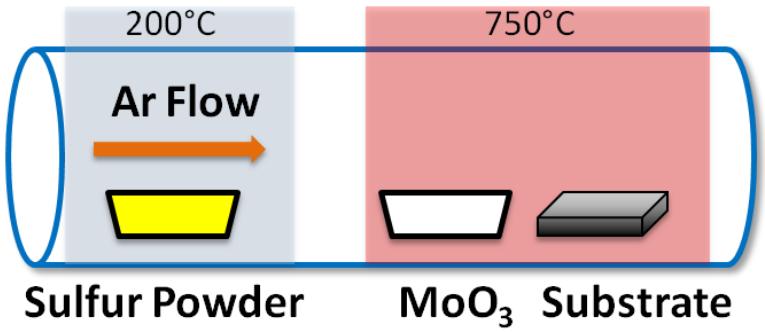

b

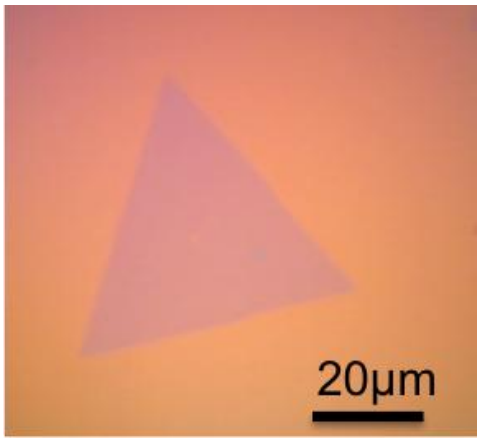

c

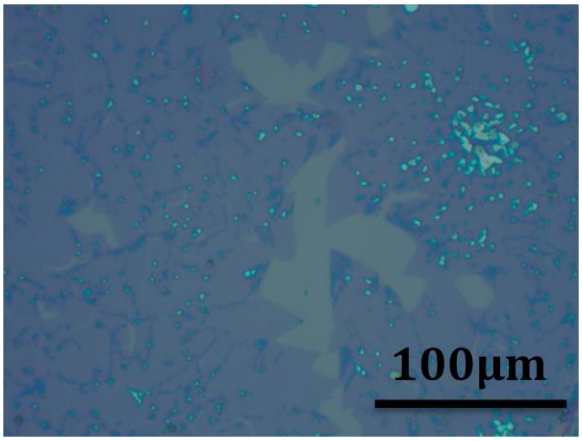

Figure 2.5 (a) The schematic illustration of CVD setup for MoS_2 growth. (b) The CVD grown MoS_2 in the shape of triangle. (c) The CVD-grown MoS_2 in continuous films.

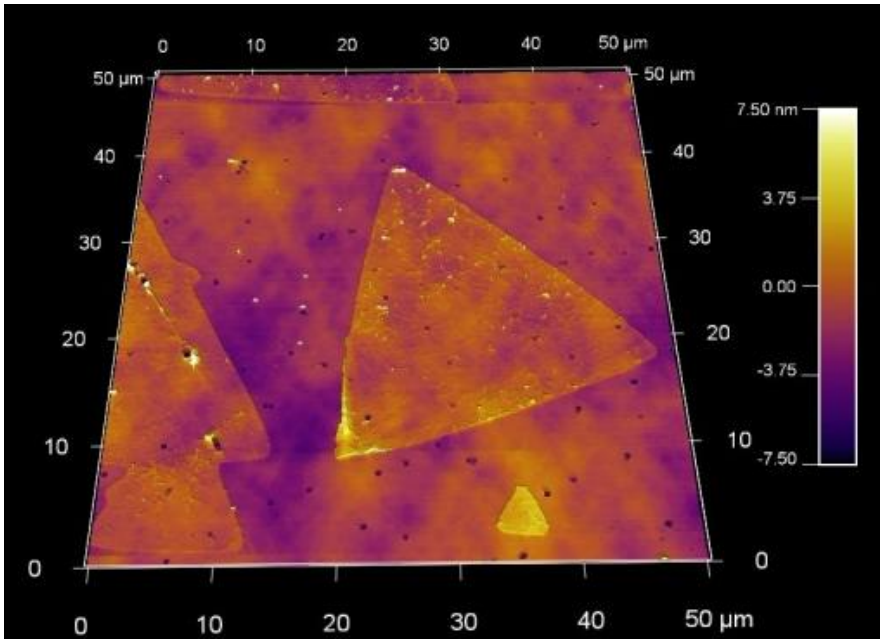

Figure 2.6 The surface morphology of MoS_2 films acquired by AFM scanning.

a

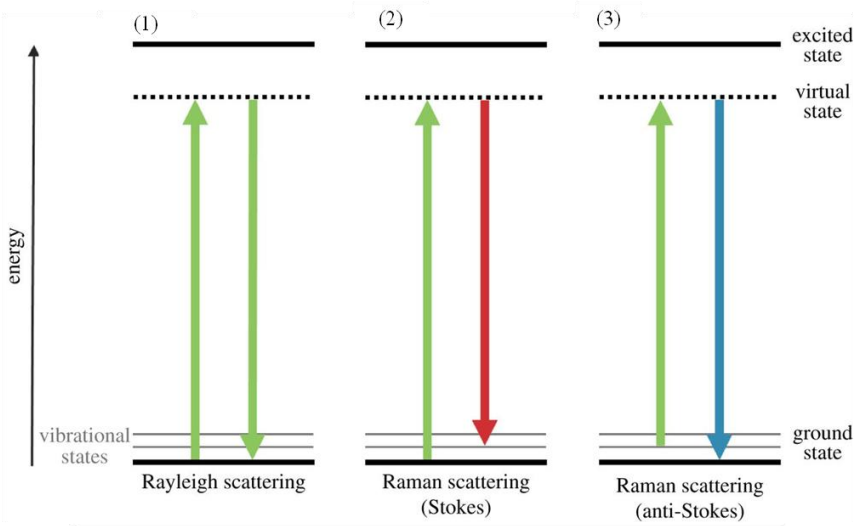

b

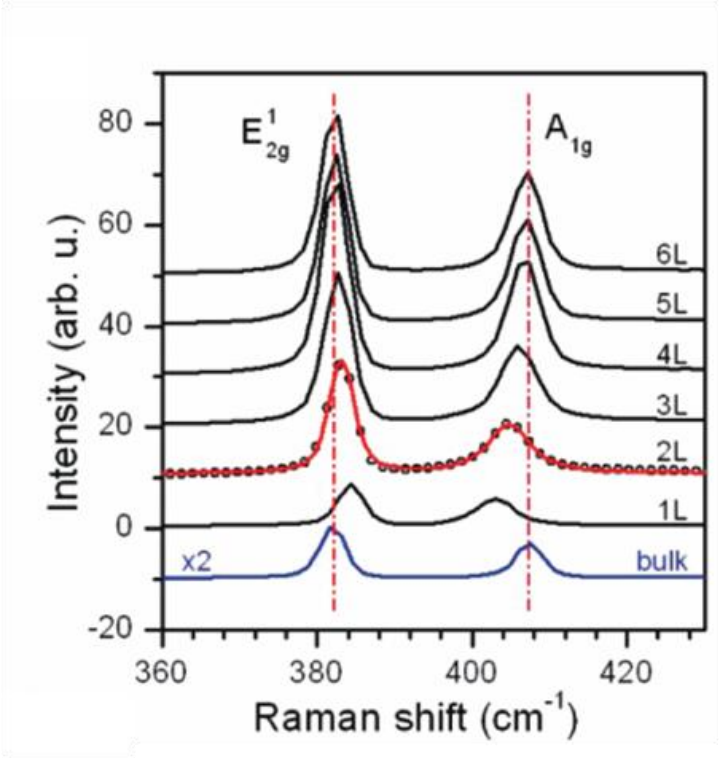

Figure 2.7 (a) The diagram of Raman scattering and Rayleigh scattering process [78]. (b) Raman spectra of MoS_2 for various thicknesses from monolayer to bulk [79].

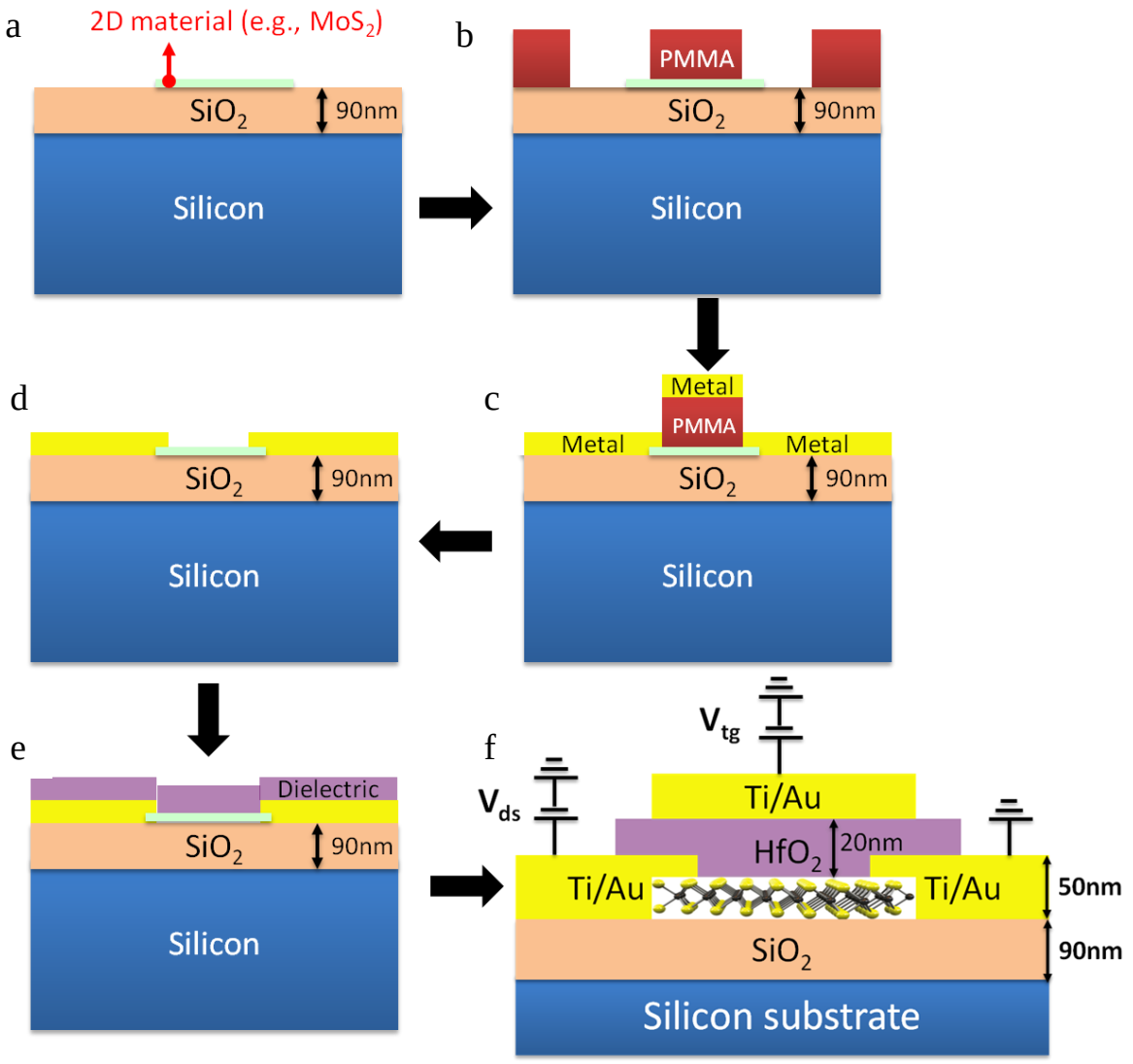

Figure 2.8 The process flow of 2D-material based device fabrication. (f) The cross view of a complete device with 2D material as the channel, HfO_2 as the gate dielectric and Ti/Au as the metal contacts (not at scale).

Figure 2.9 The device characterization system - probe station.

a

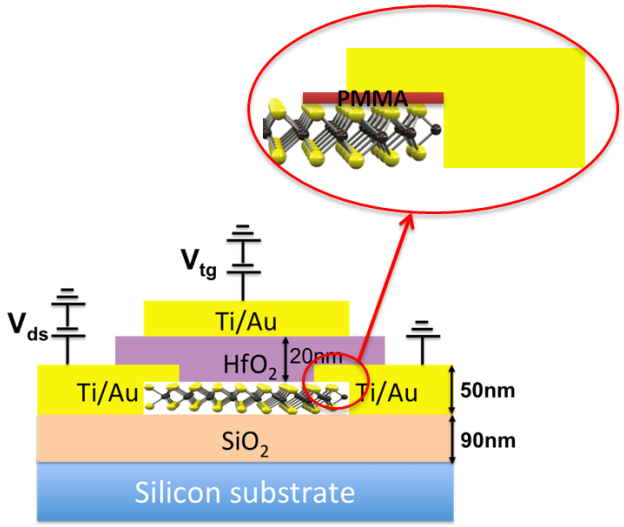

b

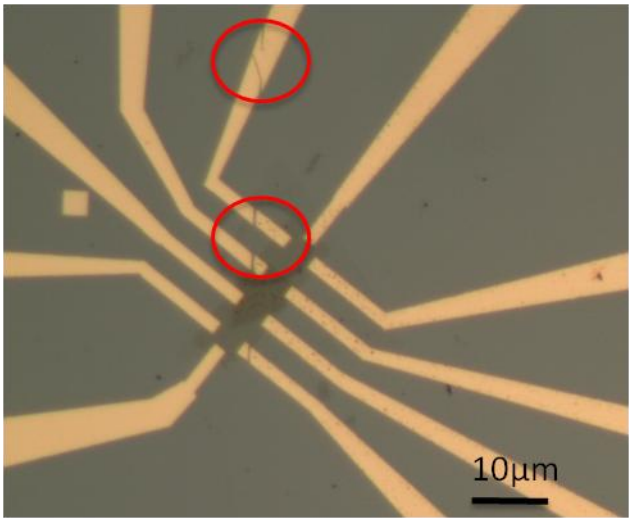

Figure 2.10 (a) Contact issue in the device arising from the PMMA residual as the zoon-in inset demonstrates. (b) Disconnected contacts (circled in red) and open circuit issue in the device arising from the fabrication process.

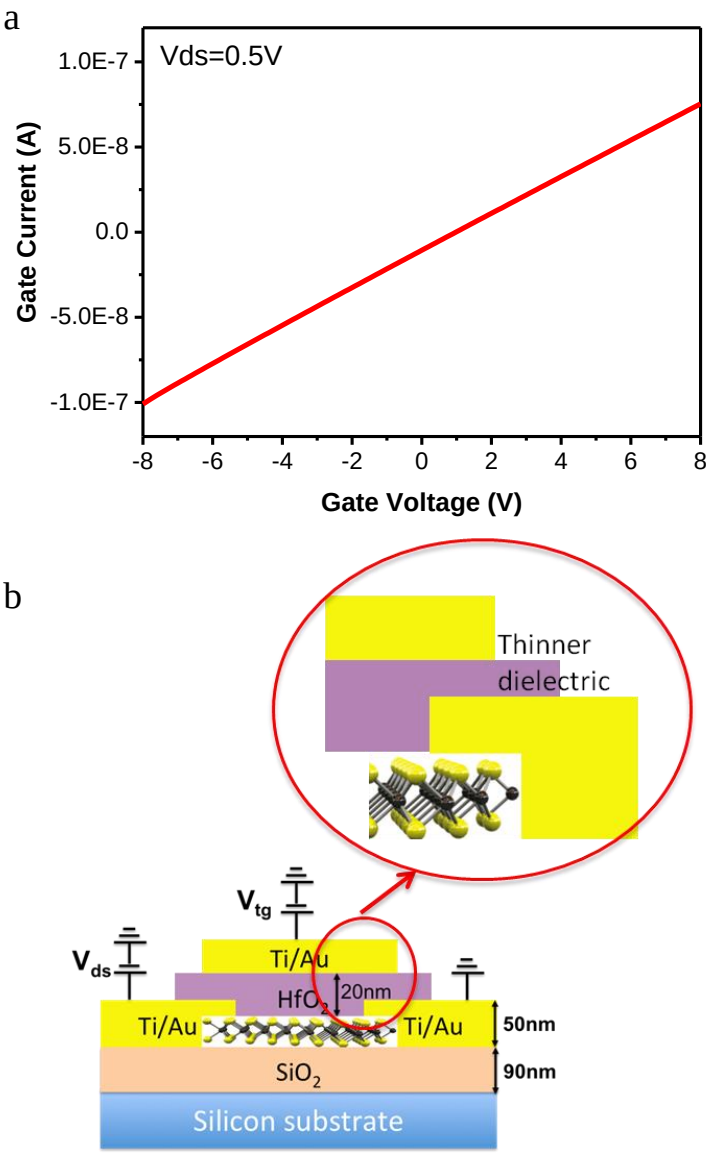

Figure 2.11 (a) High gate leakage current which may result from (b) the relatively thin gate dielectric in the overlap region between gate and drain/source as the zoon-in inset demonstrates.

Chapter 3 MoS_2 and WS_2 Heterostructure

3.1 Introduction

As discussed in chapter 1, 2D materials are layered materials bonded by the weak van der Waals force. With the absence of surface dangling bonds, heterostructures based on 2D materials can be easily formed and stacked up in a desirable order to take advantage of each component 2D material. Thus, they offer an appealing platform to build various electronic and optical devices as required in the applications, and the issue of lattice mismatch is not a concern in the construction of 2D material heterostructures, unlike in bulk material heterostructures [7].

In addition to MoS_2, other transition metal dichalcogenides (TMDs), such as WS_2, $MoSe_2$ and WSe_2, were reported to possess similar properties [36, 49, 84]. Theoretical simulation predicted that a heterostructure system consisting of monolayer MoS_2 and monolayer WS_2 forms a type II band alignment [85]. Figure 3.1 (a) illustrates the type II band alignment where it potentially has an interband transition between the valence band of WS_2 and the conduction band of MoS_2 with a reduced energy of around 1.2 eV, smaller than both of the bandgap energies in MoS_2 and WS_2. In experiment, a CVD-grown vertical MoS_2/WS_2 heterostructure was claimed to observe a strong excitonic peak in PL for the first time due to the sharp and clean interfaces between MoS_2 and WS_2, suggesting a reduced energy transition in the type II structure [73]. Moreover, the atomically sharp interface and type II structure enable a promising application for tunneling transistors by utilizing the interband transition and the band offset. Positively biasing MoS_2 moves the band and triggers the interband tunneling as shown in Figure 3.1 (b), and negative differential resistance (NDR) was observed in the MoS_2/WSe_2 heterostructure [86].

This atomically sharp interface in the heterostructure system also promotes fast and efficient carrier separation. MoS_2/WS_2 heterostructure was reported to

observe ultra-fast charge separation, and holes were transferred from the MoS_2 to WS_2 in less than 50 femtosecond after the optical excitation took place in the top MoS_2 layer as shown in Figure 3.2 [87]. Similarly, this ultra-fast carrier separation was also observed in $MoS_2/MoSe_2$ heterostructure, which leads to the formation of indirect exciton [88].

Thus, the TMD heterostructures with type II band alignments enable promising applications for novel electronics and optoelectronics for light harvesting and detection, such as tunneling transistors, photodetectors, etc.

However, the explorations of novel devices based on the TMDs heterostructures are still in the early stage. Moreover, the influence of interlayer coupling on carrier transport and distribution in the TMDs heterostructure system are not clear. This chapter will discuss the identification of MoS_2/WS_2 heterostructure by the characterizations of AFM, Raman and PL and intend to study the influence of interlayer coupling from the perspective of a Hall-bar transistor by using the MoS_2/WS_2 heterostructure as the channel.

3.2 Characterization of WS_2/MoS_2 Heterostructures

So far, the TMD heterostructures have been grown successfully by CVD [73, 75, 89]. Figure 3.3 (a) shows an optical image of MoS_2/WS_2 heterostructure with denoted spots and areas for the subsequent Raman and PL characterizations. This MoS_2/WS_2 heterostructure was grown using a similar CVD setup as shown in Figure 2.5 (a) and the exact growth schematic illustration can be found in reference [89], where the precursors, MoO_3 and WO_3, were placed in the furnace simultaneously in the high temperature zone and successful growth was done by precisely controlling the reactant flux, gas flow and temperature.

Figure 3.3 (a) shows an optical image of a sample with MoS_2/WS_2 heterostructure. Raman, PL and AFM were taken at location 1, 2 and 3. As shown in Figure 3.3 (b), the Raman spectrum of spot 1 has two Raman peaks at

352 cm^{-1} and 418 cm^{-1} that are typical peaks of WS_2 [90], suggesting that the spot 1 is the material WS_2. The Raman spectrum of spot 3 has two Raman peaks at 384 cm^{-1} and 408 cm^{-1} that are typical peaks of MoS_2 [79], suggesting that the spot 3 is the material MoS_2. Interestingly, the Raman spectrum of spot 2 has four Raman peaks, including both of WS_2 and MoS_2, which indicates that spot 2 is on the MoS_2/WS_2 vertical heterostructure.

PL spectra are used to identify the monolayer and non-monolayers in the MoS_2/WS_2 heterostructure. As discussed in chapter 1, PL is a good indicator of 2D TMDs monolayer and non-monolayers because of the direct bandgap in monolayer and indirect bandgaps in non-monolayers. Figure 3.3 (c) shows the PL spectra at location 1, 2 and 3. Spot 1 exhibits a strong PL peak at 1.96 eV, which corresponds to the bandgap of monolayer WS_2 [73]. Spot 3 exhibits a strong PL peak at 1.84 eV, which corresponds to the bandgap of monolayer MoS_2 [27, 73]. However, spot 2 exhibits a negligible PL signal compared to that of spot 1 and 3, implying that spot 2 is not monolayer.

To further investigate the thickness and structures of this MoS_2/WS_2 heterostructure system, AFM scanning and line profile measurements are performed. Figure 3.4 (a) is an optical image of a sample containing MoS_2/WS_2 heterostructure and Figure 3.4 (b) is the corresponding AFM image with line profile measurements as denoted in blue (spot 2) and red (spot 3). As shown in Figure 3.4 (c), the thickness of variation from the line profile measurement in spot 2 gives a clear step of 0.8 nm that is the thickness of monolayer 2D TMDs. In combination with the analysis of the PL and Raman spectra, one can see that the structure of spot 2 is a vertical monolayer-MoS_2/monolayer-WS_2 heterostructure, as illustrated in Figure 3.4 (e). However, there is no obvious step in the line profile measurement in spot 3 as shown in Figure 3.4 (d), suggesting the number of layers does not change across the interface in spot 3. This indicates that spot 3 is a lateral monolayer-MoS_2/monolayer-WS_2 heterostructure, as illustrated in Figure 3.4 (f).

With the examinations from Raman spectra, PL spectra and AFM scanning, the materials and structures of the MoS_2/WS_2 heterostructure have been precisely identified. The next step is to utilize these MoS_2/WS_2 heterostructures as the channel materials to fabricate devices and study the carrier transport and distribution in the MoS_2/WS_2 heterostructures.

3.3 WS_2/MoS_2 Heterostructure Devices

Figure 3.5 (a) shows an optical image of a bottom-gated Hall-bar transistor based on a MoS_2/WS_2 heterostructure. The structure is characterized by the same techniques discussed in the last section of this chapter, and it is proven that this material is a vertical monolayer-MoS_2/monolayer-WS_2 heterostructure. Figure 3.5 (b) is the schematic illustration of device structure with contacts and sensing terminals corresponding to that in Figure 3.5 (a). In addition to the drain and source contacts, there are other four pairs of sensing terminals that are arranged along the channel with equal spacing between them for the Hall-effect measurements. The sensing terminals T1 and T4 are in contact with the bottom monolayer WS_2 while T2 and T3 with the top monolayer MoS_2.

The MoS_2/WS_2 heterostructure was grown by CVD and then transferred to the SiO_2/Si substrate. The device was fabricated by the standard process discussed in chapter 2. After the deposition of the top dielectric HfO_2 by ALD and top gate metal Ti/Au, the top-gated device generates the output characteristics and transfer characteristics in Figure 3.6 (a) and (b), respectively. The linear relationship between drain current versus drain voltage indicates that the contact material Au forms an ohmic contact to WS_2, which is consistent with the previous report [3]. With positively increasing top gate biasing voltages, the device has increasing drain current, i.e., the device is an n-channel transistor. The fact that there is no intentional doping in the MoS_2/WS_2 heterostructure indicates that MoS_2 and WS_2 are naturally n-type doped. Given that the gate length-to-width ratio L/W is 3.37, the gate dielectric capacitance per unit area for 20 nm thick HfO_2 (ε_r = 19.5) is Ci = $8.63*10^{-8}$ F/cm^2, the extracted field-

effect mobility is about 1 $cm^2/(V•s)$. The ON/OFF ratio is up to 10^4 and the subthreshold swing (SS) is ~ 500 mV/dec. Those parameters indicate that the performance of the MoS_2/WS_2 heterostructure still needs improvement. However, the purpose of this MoS_2/WS_2 heterostructure device is to investigate the fundamental physical properties of MoS_2/WS_2 heterostructure, such as the carrier transport and distribution along the channel under the influence of interlayer coupling.

3.4 Summary

We systematically characterized the MoS_2/WS_2 heterostructures grown by CVD using Raman spectra, PL spectra and AFM. Vertical and lateral MoS_2/WS_2 heterostructures are identified. Vertical monolayer-MoS_2/monolayer-WS_2 heterostructures are used to fabricate Hall-bar devices with the process developed in chapter 2. In order to study the fundamental physical properties of MoS_2/WS_2 heterostructure under the influence of interlayer coupling, the Hall-effect measurements using different combinations between the sensing terminals need to be done in the further investigations. The unique properties of 2D TMD vertical heterostructures can be used for novel electronic and optoelectronic devices including high-speed photodetectors and tunneling field-effect transistors.

3.5 Figures

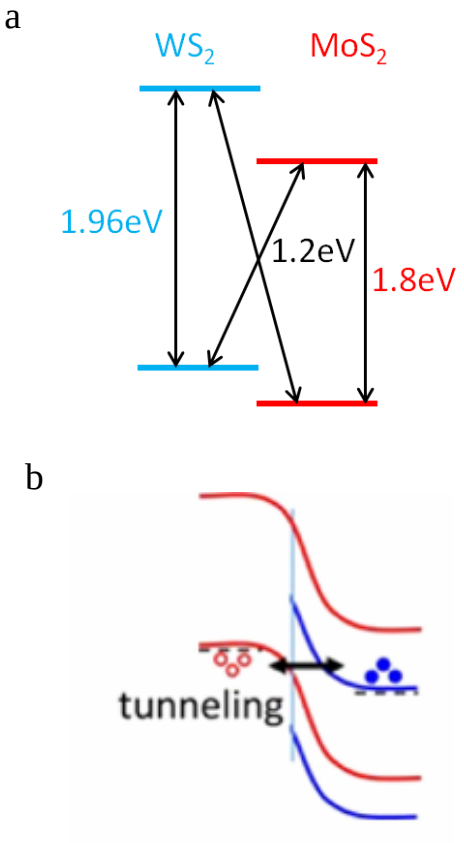

Figure 3.1 (a) A type II band alignment formed by WS_2/MoS_2 heterostructure. (b) The band diagram MoS_2/WSe_2 heterostructure with illustration of interband tunneling [86].

a

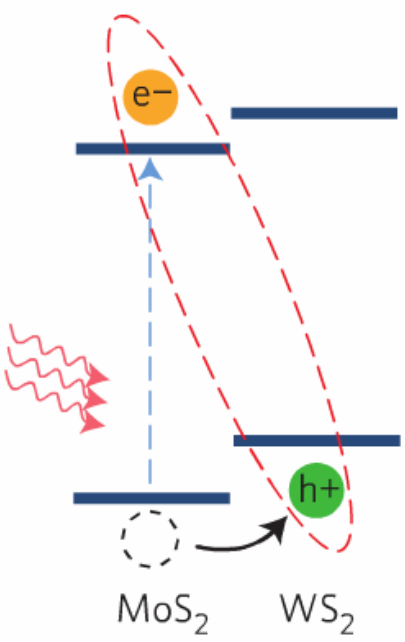

b

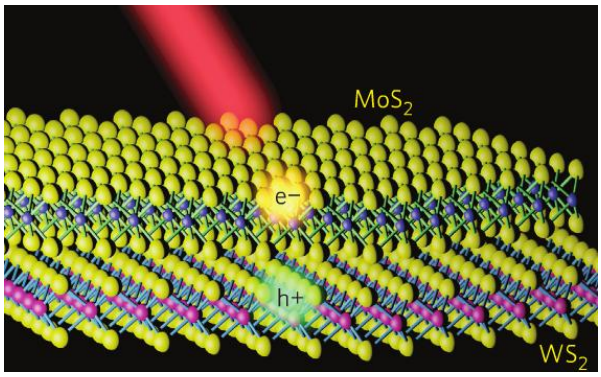

Figure 3.2 (a) The electron and hole separation resulting from the optical excitation in MoS2 with the type II band alignment. (b) The demonstration of optical excitation in MoS2 and electron and hole separation in MoS2/WS2 heterostructure. [87]

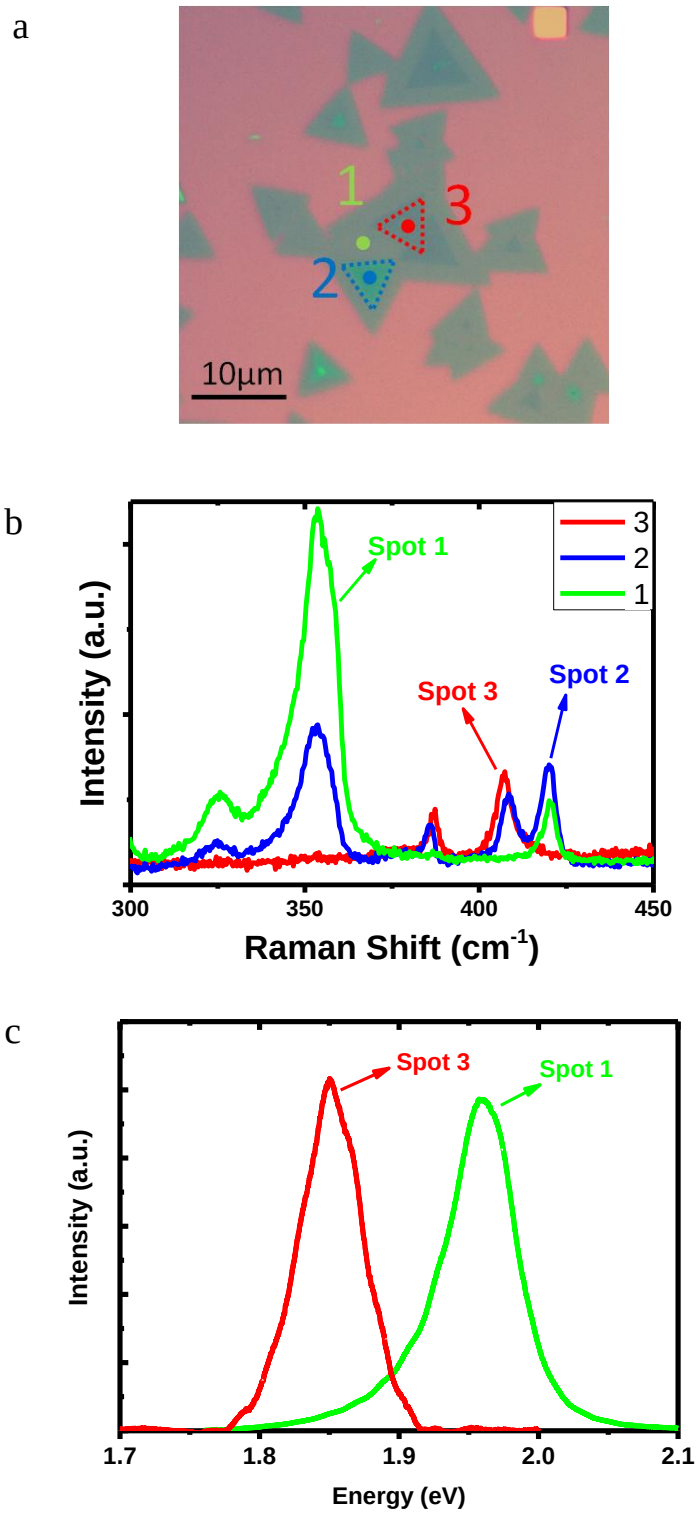

Figure 3.3 (a) An optical image of MoS_2/WS_2 heterostructure with denoted spots and areas for Raman and PL characterizations. (b) The Raman spectra in spots 1, 2 and 3. (c)The PL spectra in spots 1 and 3 with negligible signal in spot 2.

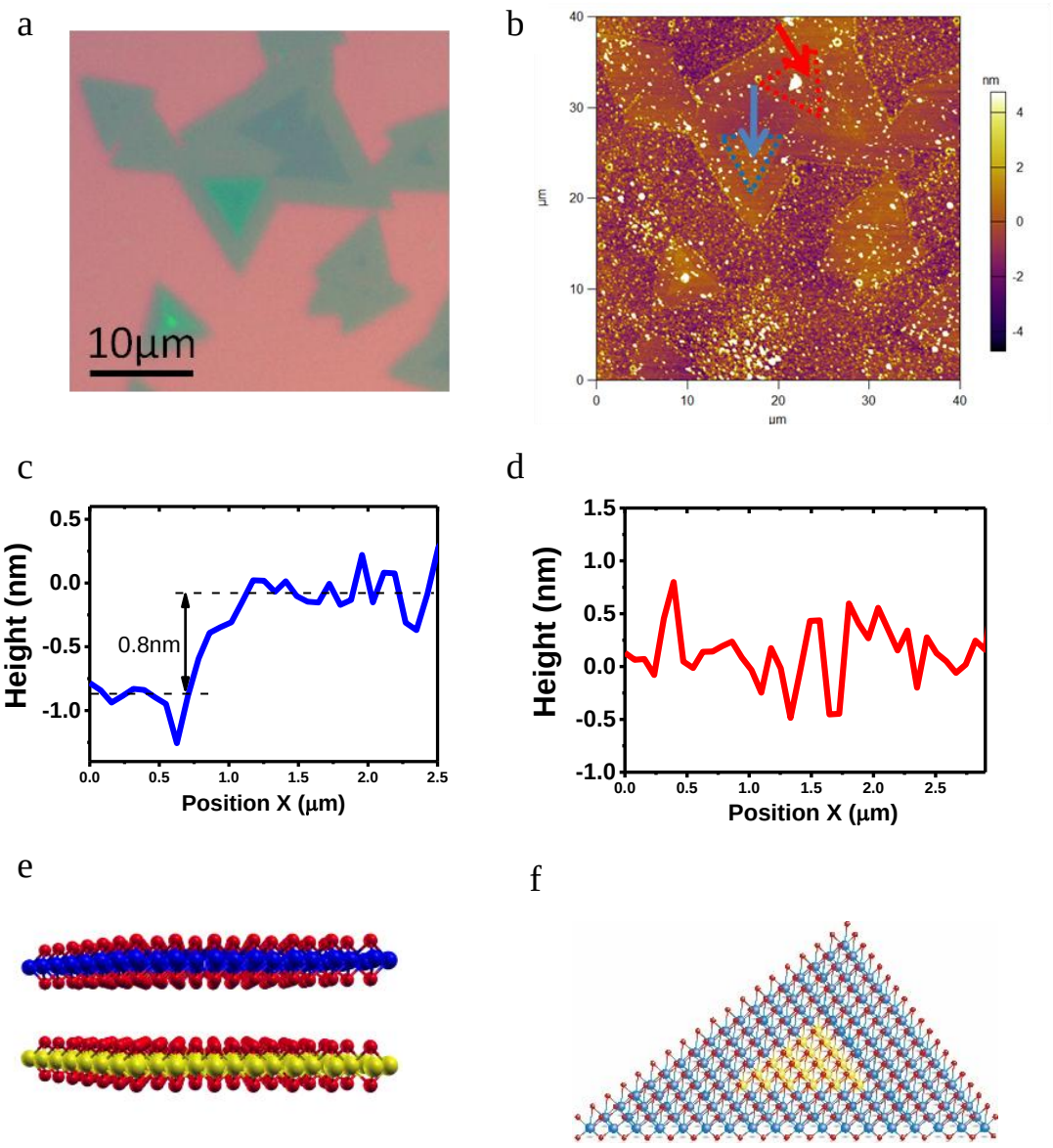

Figure 3.4 (a) An optical image of MoS_2/WS_2 heterostructure the same as Figure 3.3 (a) without the denoted labels. (b) An AFM scanning image corresponding to Figure 3.4 (a) with line profile measurements as denoted in blue (spot 2) and red (spot 3). (c) The height variation from the line profile measurement denoted in the blue arrow. (d) The height variation from the line profile measurement denoted in the red arrow. (e) Illustration of vertical monolayer-MoS_2/monolayer-WS_2 heterostructure. (f) Illustration of lateral monolayer-MoS_2/monolayer-WS_2 heterostructure.

a

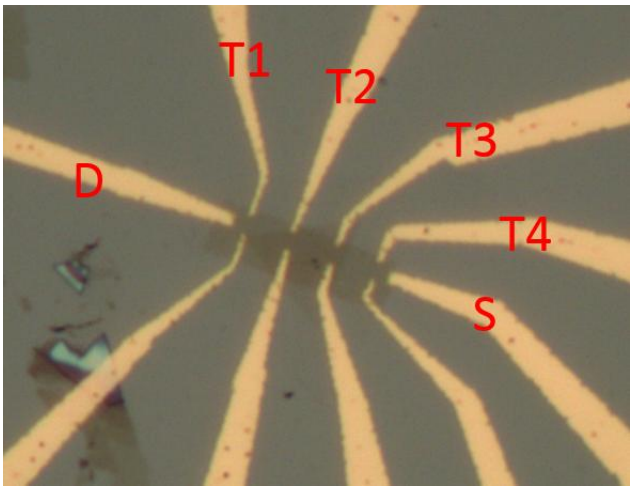

b

Figure 3.5 (a) An optical image of a Hall-bar transistor based on a vertical monolayer-MoS_2/monolayer-WS_2 heterostructure. The sensing terminals T1 and T4 are in contact with the bottom monolayer WS_2 while T2 and T3 with the top monolayer MoS_2. (b) Schematic illustration of the device structure in (a).

a

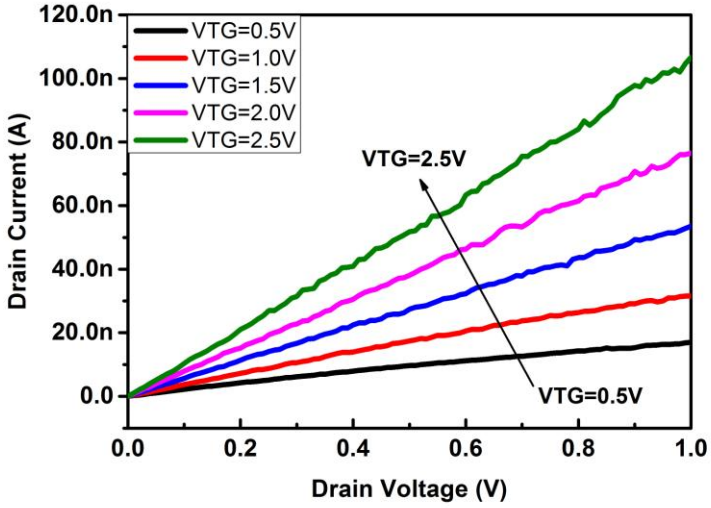

b

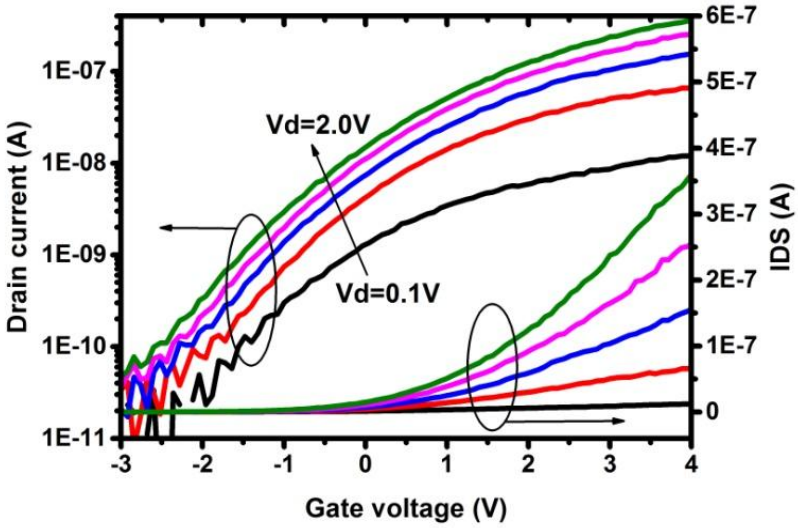

Figure 3.6 (a) The output characteristics and (b) transfer characteristics of the MoS_2/WS_2 heterostructure.

Chapter 4 Anisotropic Germanium Selenide

4.1 Introduction

Black phosphorus has been a rising star in 2D layered materials since its emergence in 2014. A remarkable field-effect transistor with black phosphorus a few nanometers thick as the channel material was reported [91], and since then it has attracted extensive attention and opened a new era for this long-standing elemental material, phosphorus, in a new form as a 2D layered material. The black phosphorus field-effect transistor exhibits on/off ratios of 10^5 and a field effect mobility up to 1000 $cm^2/(V•s)$ at room temperature, enabling this new elemental black phosphorus to be promising for nanoelectronic applications [91].

Like other 2D layered materials, black phosphorus has also thickness-dependent direct bandgap, ranging from 0.3 eV in bulk to 1.5 eV in monolayer [92, 93], as shown in Figure 4.1 (a) [94]. This widely tunable and direct bandgap of black phosphorus fills the window gap in bandgap energies between graphene and 2D TMDs and makes it a promising candidate for infrared optoelectronic applications.

The 2D layered black phosphorus has an anisotropic crystal structure as shown in Figure 4.1 (b) [95]. It is an orthorhombic, buckled honeycomb structure with each atom having three neighboring atoms, and the weak van der Waals force between layers also enables it to be exfoliated mechanically [95]. It has armchair and zigzag edges in two perpendicular directions within one plane. Thus, the electrical and optical properties of black phosphorus demonstrate strongly angle-dependent behaviors due to this in-plane anisotropic structure. Black phosphorus was reported to possess a higher Hall mobility for holes in the armchair direction with light effective mass, nearly twice the mobility in the zigzag direction [96]. The monolayer black phosphorus was observed to have strongly anisotropic excitons with a large binding energy [97]. Moreover, it is also found

that black phosphorus demonstrated anisotropic property in thermal conduction with larger thermal conductivity along the zigzag direction, which is ascribed to the anisotropic phonon dispersion and group velocities [98, 99].

As a compound semiconductor material, germanium selenide (GeSe) in bulk has a similar crystal structure to black phosphorus, as shown in Figure 4.1 (c). As a group-IV mono-chalcogenide, GeSe has a distorted rocksalt (d-NaCl) crystal structure with eight atoms in a unit cell [100]. The layers of GeSe are bonded by van der Waals force in an orthorhombic structure with space group Pnma at room temperature [101, 102]. Bulk GeSe was reported to have an indirect band gap of 1.07 eV [103] and monolayer GeSe was found to have a direct band gap with small effective mass of carriers [102]. Thus, 2D layered GeSe exhibits promising applications in photovoltaics, thermoelectrics, and photodetectors [104-106]. Similar to black phosphorus, 2D layered GeSe also has anisotropic crystal structure. In this project, the dependence of electronic transport on the crystal orientation is systematically studied by polarized Raman spectroscopy and angle-resolved conductance measurement.

4.2 Angle-resolved Electrical Conductance

In order to study the anisotropic conductance of layered GeSe, an electrical device is made using the fabrication process with E-beam lithography discussed in chapter 2 and angle-resolved DC electrical conductance measurement is executed. As seen in Figure 4.2 (a), this device has 6 pairs of electrodes and each electrode has a spacing of $30\,^{\circ}$ apart. The pair of electrode T1 is defined as the $0\,^{\circ}$ reference line. An electric field is applied across each pair that is diagonally positioned and the DC conductance measurement at a certain degree with respect to T1 is performed. The layered GeSe shows a p-type electrical behavior and the DC conductance measurement is performed with drain voltage of 1 V and bottom gate voltage of -5 V at room temperature. As shown in Figure 4.2 (b), the data points in black are from the electrical measurement while the

red line is the fitting. It shows that the maximum conductance is along the T5 direction and layered GeSe demonstrates anisotropic electrical property.

4.3 Polarized Raman Spectroscopy

It has been demonstrated that polarized Raman spectroscopy is an effective and quick technique to determine the crystal orientation (i.e., armchair direction and zigzag direction) in black phosphorus by taking advantages of polarization-dependent A_g mode and B_{2g} mode [107, 108]. Similarly, with the anisotropic crystal structure the armchair direction and zigzag direction in GeSe can also be identified by the polarized Raman spectroscopy.

The setup of the polarized Raman spectroscopy is illustrated in Figure 4.3 (a). A 532 nm laser is used as the excitation light source. Firstly, it goes through a wave plate before it reaches the layered GeSe flake materials. After that, the scattered light goes through a receiver polarizer and then is collected and analyzed by a spectrum analyzer, and the polarized Raman spectra are produced. Figure 4.3 (b) depicts the indicative directions with an exfoliated GeSe flake that corresponds to Figure 4.3 (a). Since the receiver polarizer is fixed and not rotational, the scattered light is always pointing along the horizontal direction. The wave plate can be rotated and make the incident light polarized with an angle Θ, called rotation angle, with respect to the horizontal direction. Initially, the wave plate is positioned parallel to the polarizer, i.e., $\Theta = 0°$. Since the purpose of this polarized Raman spectroscopy is to determine the armchair direction and zigzag direction that are unknown, the armchair direction is assumed to have the denoted direction and the angle between armchair and the horizontal direction is Φ, called orientation angle. Once the sample is positioned for the polarized Raman measurement, the orientation angle Φ is fixed and ready for analysis and identification. The perpendicular direction to the armchair is the zigzag direction. By rotating the wave plate from 0 to 180 degrees with a 10 degrees step, the scattered light is analyzed and corresponding angular dependent Raman spectra in polar plots are generated as shown in Figure 4.3 (a).

Figure 4.4 depicts the Raman spectrum of layered GeSe acquired from unpolarized Raman scattering measurement setup. It has clearly typical Raman peaks at 83 cm^{-1} and 189 cm^{-1} corresponding to the A_g modes while the peak at 152 cm^{-1} belongs to the B_{3g} mode, which is consistent with the previous report about the bulk GeSe [100].

In order to identify the crystal orientation, the experimental data is fitted using a simple model and the orientation angle Φ is then extracted. For quantitative analysis, it is necessary to introduce the unit vectors $\mathbf{e_i}$ for the incident light and $\mathbf{e_s}$ for the scattered light with respect to the assumed armchair direction. As seen in Figure 4.4 (b), $\mathbf{e_i} = (0 \ \cos(\Theta+\Phi) \ \sin(\Theta+\Phi))$ and $\mathbf{e_s} = (0 \ \cos\Phi \ \sin\Phi)$. Since GeSe has a D_{2h} space group, the Raman tensors of A_g mode and B_{3g} mode are [109]:

$$R(A_g) = \begin{pmatrix} a & 0 & 0 \\ 0 & b & 0 \\ 0 & 0 & c \end{pmatrix} \text{ and } R(B_{3g}) = \begin{pmatrix} 0 & 0 & 0 \\ 0 & 0 & g \\ 0 & g & 0 \end{pmatrix}.$$

The Raman cross section is written as [110]:

$$S \propto (\mathbf{e_i} \bullet R \bullet \mathbf{e_s})^2,$$

where R is the Raman tensor, $\mathbf{e_i}$ and $\mathbf{e_s}$ are the unit vectors for the incident and scattered light, respectively.

Thus, the Raman scattering intensity can be written as

$$I(A_g) = (b \bullet \cos(\Theta+\Phi) \bullet \cos\Phi + c \bullet \sin(\Theta+\Phi) \bullet \sin\Phi)^2,$$

$$I(B_{3g}) = (g \bullet \sin(\Theta+2\Phi))^2.$$

Thus, the Raman scattering intensity of A_g mode and B_{3g} mode are strongly dependent on the rotation angle Θ and orientation angle Φ.

Figure 4.5 (a) illustrates a polar plot of measured and fitted A_g mode (189 cm^{-1}) and B_{3g} mode (152 cm^{-1}) as a function of rotation angle Θ. The solid lines are

based on the above Raman scattering intensity calculations. Fitting the A_g mode (189 cm^{-1}) and B_{3g} mode (152 cm^{-1}) simultaneously leads to $\Phi = 30°$ approximately. Figure 4.5 (b) shows an optical image of the GeSe flake in a position during the polarized Raman measurement. The fitted $\Phi = 30°$ with respect to the horizontal line gives the armchair direction as denoted by the red line. The armchair direction nearly overlaps with the direction of T5 which has the maximum conductance. However, this conclusion was not confirmed with repeatable results from angle-resolved polarized Raman measurements and they gave the armchair along other directions rather than the direction of T5. Thus, further confirmation with repeatable experimental results is needed.

4.4 Summary

Black phosphorus exhibits strongly angle-dependent behaviors in electrical and optical properties due to its in-plane anisotropic structure. With crystal structure analogous to that of black phosphorus, the anisotropic electrical and optical properties of a novel layered material, GeSe, are explored in this chapter. An electrical device with 6 pairs of electrodes spaced at 30 ° apart is used to study the angle-resolved DC electrical conductance, and the maximum conductance is along the T5 direction. Polarized Raman spectroscopy is used to determine the crystal orientation. The polarized Raman measurement is performed with a rotational wave plate for the incident light while keeping the sample and a receiver polarizer for the scattered light fixed. By fitting the measured data with the calculated results, the armchair direction is identified. The armchair direction approximately overlaps with the direction of T5 which has the maximum conductance. But this conclusion needs further confirmation with repeatable angle-resolved conductance and polarized Raman spectra measurements. The anisotropic electrical and optical properties make the newly studied layered GeSe materials promising for novel electronic and optoelectronic applications in the future.

4.5 Figures

a

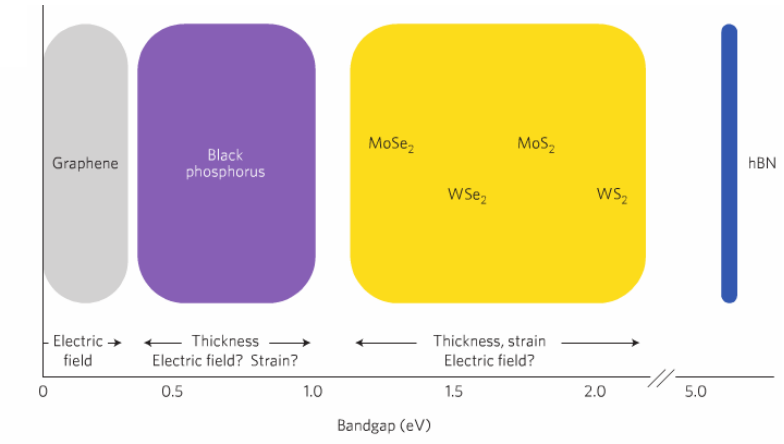

b

c

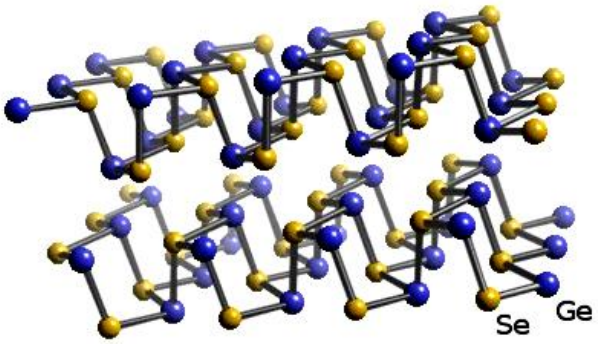

Figure 4.1 (a) The map of bandgap energies of various 2D materials [94]. The bandgap of black phosphorus in various thicknesses fills the window gap in bandgap energies between graphene and TMDs. (b) The atomic structure of few-layer black phosphorus [95]. (c) The atomic structure of germanium selenide, similar to black phosphorus [111].

a

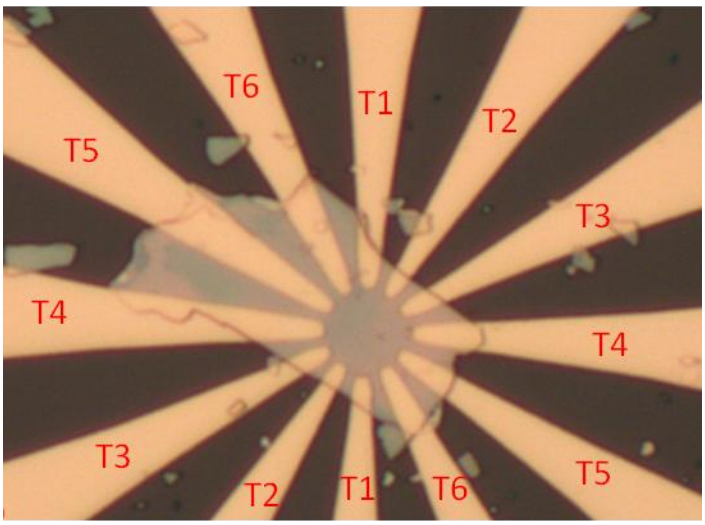

b

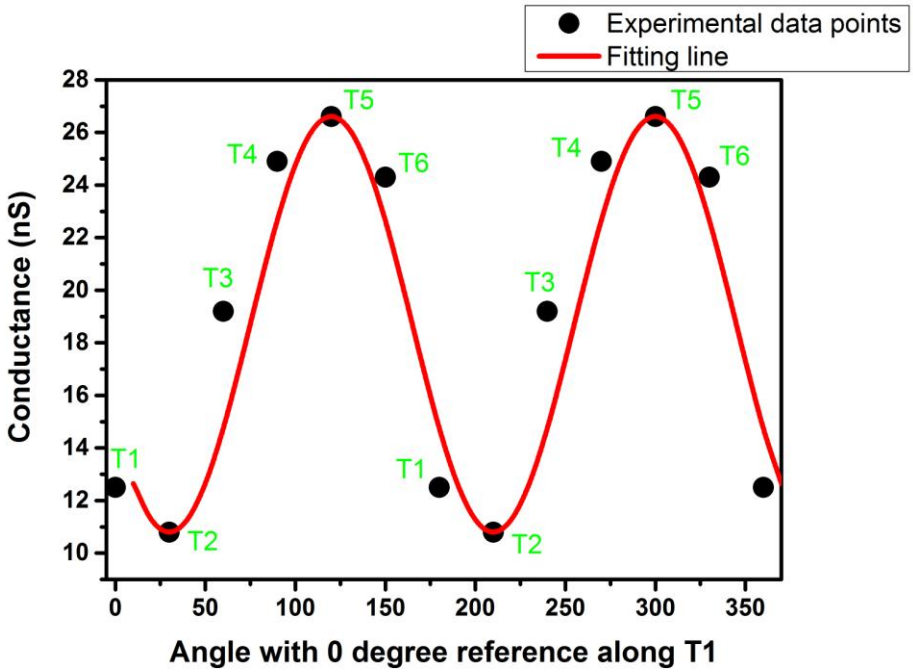

Figure 4.2 (a) The electrical device with 6 pairs of electrodes for angle-resolved DC conductance measurement. (b) The angle-resolved DC conductance at room temperature with a 0° reference line along the electrodes T1. The data points are from the measurement with a pair of denoted electrodes while the red is the fitting line from calculation.

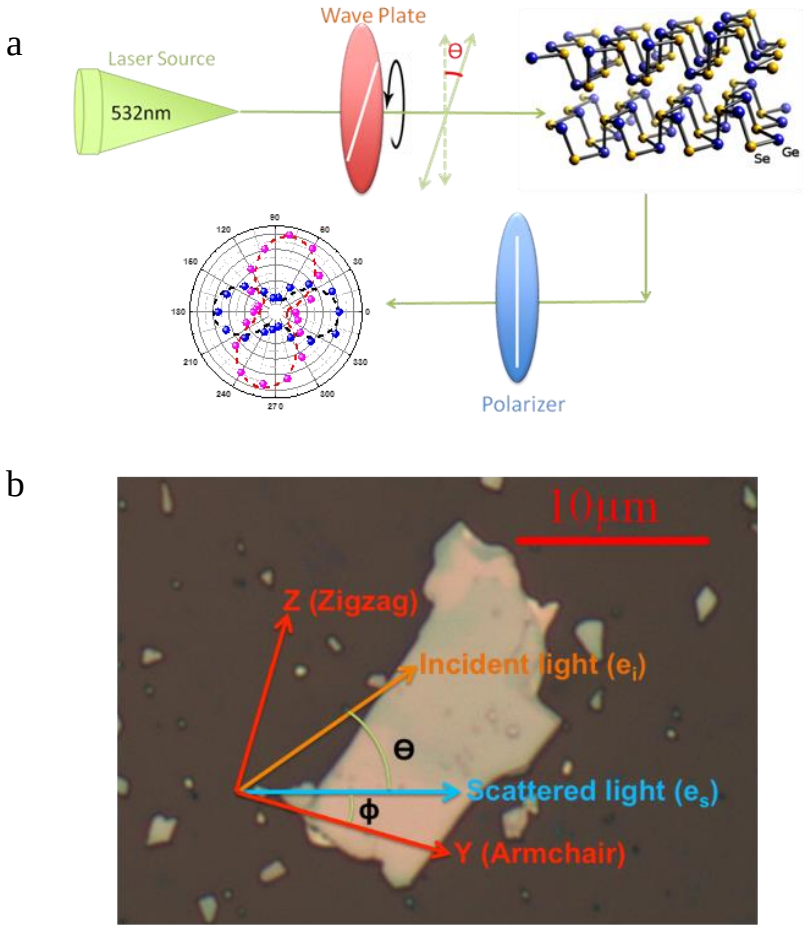

Figure 4.3 (a) The schematic setup for polarized Raman spectra measurement. (b) The indicative directions with an exfoliated GeSe flake. The scattered light is fixed at the horizontal direction. The direction of incident light can be rotated with respect to the horizontal direction and the angle between them is denoted as Θ. The armchair and zigzag are assumed to have the denoted directions and the angle between armchair and the horizontal direction is Φ.

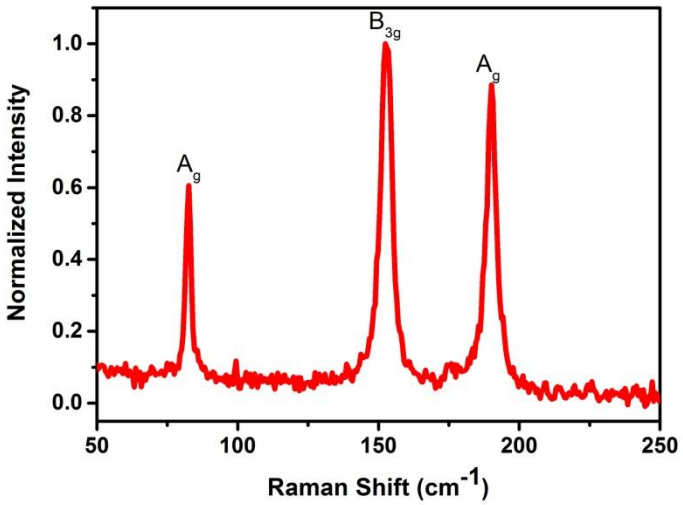

Figure 4.4 The Raman spectrum of layered GeSe.

a

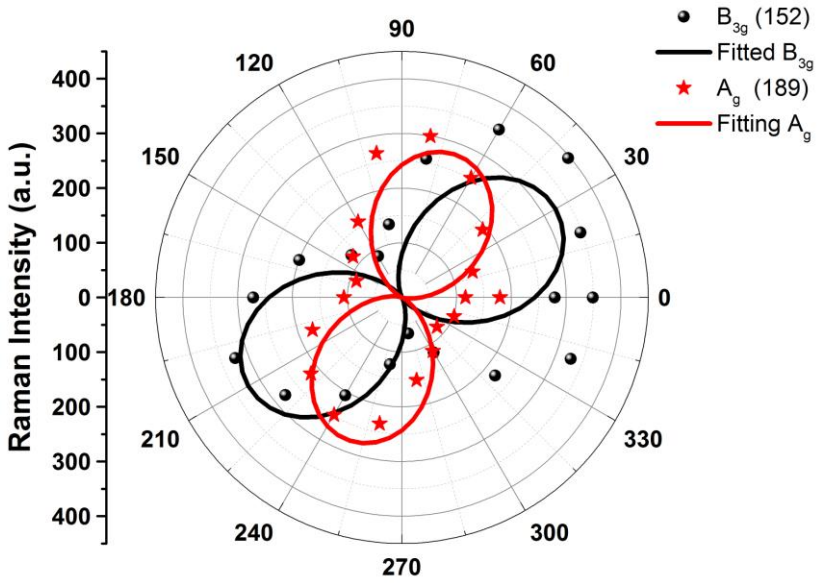

b

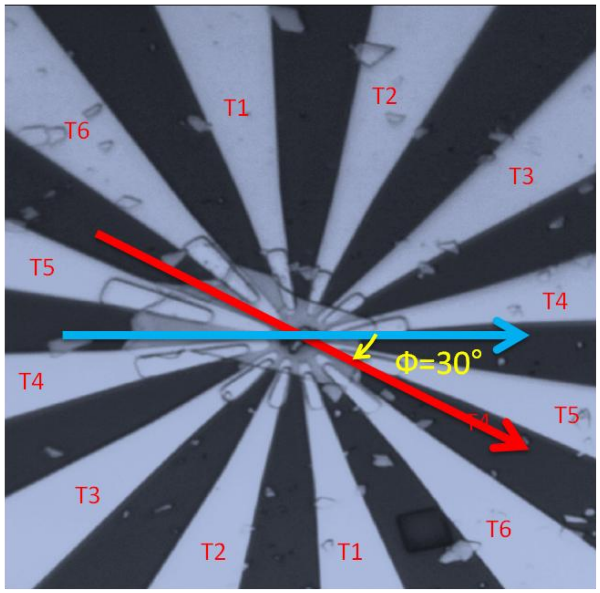

Figure 4.5 (a) A polar plot of measured and fitted A_g mode (189 cm^{-1}) and B_{3g} mode (152 cm^{-1}) as a function of rotation angle Θ. (b) An optical image of the GeSe flake in a position during the polarized Raman measurement that is used to figure out the crystal orientation. The blue denotes the horizontal line and the red is along the armchair direction. The fitted Φ = 30° with respect to the horizontal line denotes the armchair direction.

Chapter 5 Conclusion and Future Work

Two-dimensional (2D) materials have attracted extensive attention due to their unique and remarkable properties, such as atomically thin body, pristine surface free of dangling bonds, tunable bandgap, and reasonably high mobility, which make 2D materials promising candidates for many electronic and optoelectronic devices in low power, high performance and flexible applications.

In this thesis, a complete process flow, from material preparation/ characterization to fabrication/characterization of various electronic and optoelectronic devices based on 2D materials, has been developed and optimized. Using these techniques, Hall-bar devices and transistors based on MoS_2/WS_2 heterostructures and GeSe have been successfully fabricated and characterized.

The optical and electrical properties of MoS_2/WS_2 heterostructures grown by chemical vapor deposition have been studied. The vertical and lateral MoS_2/WS_2 structures are identified by using Raman spectra, PL spectra and AFM. The devices show typical n-channel characteristics, indicating that MoS_2 and WS_2 are naturally n-type doped. By using the Hall-bar devices, Hall-effect measurements need to be done in the future to investigate the influence of interlayer coupling on the carrier transport and distribution in the MoS_2/WS_2 heterostructures. Due to the type II band alignment and sharp interface, these vertical and lateral MoS_2/WS_2 heterostructures can potentially be used for tunneling field-effect transistors and light harvesting and detection, such as high-speed photodetectors. Thus, novel electronic and optoelectronic devices based on the MoS_2/WS_2 heterostructures will be explored in the future.

In addition, the crystal orientation and electronic transport in GeSe have been also studied. An electrical device with 6 pairs of electrodes spaced at 30 ° apart is used to study the angle-resolved DC electrical conductance, and the crystallographic direction of the GeSe is determined by angle-resolved polarized

Raman measurement. The results indicate that GeSe has a prominent anisotropic electronic transport with maximum conductance likely along the armchair direction, but further confirmation with repeatable experimental results is needed. The anisotropic conductance in GeSe may enable a new series of electronic and optoelectronic devices such as plasmonic devices with resonance frequency continuously tunable with light polarization direction, and high-efficiency thermoelectric devices. These possibilities will be explored in future work.

In summary, a complete process flow for 2D materials and devices has been successfully established, and the MoS_2/WS_2 heterostructures and the anisotropic electronic transport and polarized Raman scattering in GeSe have been studied. The research in this thesis can expand knowledge of 2D materials and their heterostructures, and provide important information in designing and fabricating novel electronic and optoelectronic devices based on these materials.

References

[1] G. Fiori, F. Bonaccorso, G. Iannaccone, T. Palacios, D. Neumaier, A. Seabaugh, *et al.*, "Electronics based on two-dimensional materials," *Nature Nanotechnology*, vol. 9, pp. 768-779, 2014.

[2] K. Singh, A. Ohlan, and S. K. Dhawan, *Polymer-Graphene Nanocomposites: Preparation, Characterization, Properties, And Applications*, 2012.

[3] B. Radisavljevic, A. Radenovic, J. Brivio, V. Giacometti, and A. Kis, "Single-layer MoS_2 transistors," *Nature Nanotechnology*, vol. 6, pp. 147-150, 2011.

[4] H. Liu, A. T. Neal, and P. D. Ye, "Channel length scaling of MoS2 MOSFETs," *ACS Nano*, vol. 6, pp. 8563-8569, 2012.

[5] M. Chhowalla, D. Jena, and H. Zhang, "Two-dimensional semiconductors for transistors," *Nature Reviews Materials*, 2016.

[6] A. K. Geim and I. V. Grigorieva, "Van der Waals heterostructures," *Nature*, vol. 499, pp. 419-425, 2013.

[7] G. S. Duesberg, "Heterojunctions in 2D semiconductors: a perfect match," *Nature Materials*, vol. 13, pp. 1075-1076, 2014.

[8] Z. Liu, M. Amani, S. Najmaei, Q. Xu, X. Zou, W. Zhou, *et al.*, "Strain and structure heterogeneity in MoS_2 atomic layers grown by chemical vapour deposition," *Nature Communications*, vol. 5, p. 5246, 2014.

[9] H. J. Conley, B. Wang, J. I. Ziegler, R. F. Jr, S. T. Pantelides, and K. I. Bolotin, "Bandgap engineering of strained monolayer and bilayer MoS_2," *Nano Letters*, vol. 13, pp. 3626-3630, 2013.

[10] A. Nathan, A. Ahnood, M. T. Cole, S. Lee, Y. Suzuki, P. Hiralal, *et al.*, "Flexible electronics: the next ubiquitous platform," *Proceedings of the IEEE*, vol. 100, pp. 1486-1517, 2012.

[11] D. Akinwande, N. Petrone, and J. Hone, "Two-dimensional flexible nanoelectronics," *Nature Communications*, vol. 5, p. 5678, 2014.

[12] H. J. Yoon, J. H. Yang, Z. Zhou, and S. S. Yang, "Carbon dioxide gas sensor using a graphene sheet," *Sensors and Actuators B: Chemical*, vol. 157, pp. 310-313, 2011.

[13] H. Li, Z. Yin, Q. He, H. Li, X. Huang, G. Lu, *et al.*, "Fabrication of single- and multilayer MoS_2 film-based field-effect transistors for sensing NO at room temperature," *Small,* vol. 8, pp. 63-67, 2012.

[14] K. S. Novoselov, A. K. Geim, S. V. Morozov, D. Jiang, Y. Zhang, S. V. Dubonos, *et al.*, "Electric field effect in atomically thin carbon films," *Science,* vol. 306, pp. 666-669, 2004.

[15] C. A. H. Neto, F. Guinea, N. M. R. Peres, K. S. Novoselov, and A. K. Geim, "The electronic properties of graphene," *Reviews of Modern Physics,* vol. 81, p. 109, 2009.

[16] F. Schwierz, "Graphene transistors," *Nature Nanotechnology,* vol. 5, pp. 487-496, 2010.

[17] R. R. Nair, P. Blake, A. N. Grigorenko, and K. S. Novoselov, "Fine structure constant defines visual transparency of graphene," *Science,* vol. 320, p. 1308, 2008.

[18] A. K. Geim and K. S. Novoselov, "The rise of graphene," *Nature Materials,* vol. 6, pp. 183-191, 2007.

[19] B. Richard, J. Bjarke, N. Louis, A. Mie, R. Emile, B. Marco, *et al.*, "Bandgap opening in graphene induced by patterned hydrogen adsorption," *Nature Materials,* vol. 9, pp. 315-319, 2010.

[20] Y. Zhang, T. T. Tang, C. Girit, Z. Hao, M. C. Martin, and A. Zettl, "Direct observation of a widely tunable bandgap in bilayer graphene," *Nature,* vol. 459, pp. 820-823, 2009.

[21] Y. W. Son, M. L. Cohen, and S. G. Louie, "Energy gaps in graphene nanoribbons," *Phys. Rev. Lett.,* vol. 97, p. 216803, 2006.

[22] M. Y. Han, B. Özyilmaz, Y. Zhang, and P. Kim, "Energy band-gap engineering of graphene nanoribbons," *Phys. Rev. Lett.,* vol. 98, p. 206805, 2007.

[23] M. Y. Han, B. O ̈zyilmaz, Y. Zhang, and P. Kim, "Energy band-gap engineering of graphene nanoribbons," *Phys. Rev. Lett.,* vol. 98, p. 206805, 2007.

[24] D. Jariwala, V. K. Sangwan, L. J. Lauhon, T. J. Marks, and M. C. Hersam, "Emerging device applications for semiconducting two-dimensional transition metal dichalcogenides," *ACS Nano,* vol. 8, pp. 1102-1120, 2014.

[25] D. Xiao, G.-B. Liu, W. Feng, X. Xu, and W. Yao, "Coupled spin and valley physics in monolayers of MoS_2 and other group-VI dichalcogenides," *Physical Review Letters,* vol. 108, p. 196802, 2012.

[26] A. Splendiani, L. Sun, Y. Zhang, T. Li, J. Kim, C.-Y. Chim, *et al.*, "Emerging photoluminescence in monolayer MoS_2," *Nano Letters,* vol. 10, pp. 1271-1275, 2010.

[27] K. Mak, C. Lee, J. Hone, J. Shan, and T. F. Heinz, "Atomically thin MoS_2: a new direct-gap semiconductor," *Physical Review Letters,* vol. 105, 2010.

[28] S. Butun, S. Tongay, and K. Aydin, "Enhanced light emission from large-area monolayer MoS_2 using plasmonic nanodisc arrays," *Nano letters,* vol. 15, pp. 2700-2704, 2015.

[29] Z. Yang, R. Grassi, M. Freitag, Y.-H. Lee, T. Low, and W. Zhu, "Spatial/temporal photocurrent and electronic transport in monolayer molybdenum disulfide grown by chemical vapor deposition," *Applied Physics Letters,* vol. 108, p. 83104, 2016.

[30] K. Kaasbjerg, K. S. Thygesen, and K. W. Jacobsen, "Phonon-limited mobility in n-type single-layer MoS_2 from first principles," *Physical Review B,* vol. 85, p. 115317, 2012.

[31] N. Ma and D. Jena, "Charge scattering and mobility in atomically thin semiconductors," *Physical Review X,* vol. 4, p. 11043, 2014.

[32] X. Cui, G.-H. Lee, Y. D. Kim, G. Arefe, P. Y. Huang, C.-H. Lee, *et al.*, "Multi-terminal transport measurements of MoS_2 using a van der Waals heterostructure device platform," *Nature Nanotechnology,* vol. 10, pp. 534-540, 2015.

[33] B. Radisavljevic and A. Kis, "Mobility engineering and a metal–insulator transition in monolayer MoS_2," *Nature Materials,* vol. 12, pp. 815-820, 2013.

[34] S. Das, H.-Y. Chen, A. V. Penumatcha, and J. Appenzeller, "High performance multilayer MoS_2 transistors with scandium contacts," *Nano Letters,* vol. 13, pp. 100-105, 2012.

[35] D. Jariwala, V. K. Sangwan, D. J. Late, J. E. Johns, V. P. Dravid, T. J. Marks, *et al.*, "Band-like transport in high mobility unencapsulated single-layer MoS_2 transistors," *Applied Physics Letters,* vol. 102, p. 173107 2013.

[36] W. M. Iqbal, Z. M. Iqbal, F. M. Khan, A. M. Shehzad, Y. Seo, J. Park, *et al.*, "High-mobility and air-stable single-layer WS_2 field-effect transistors sandwiched between chemical vapor deposition-grown hexagonal BN films," *Scientific Reports,* vol. 5, p. 10699, 2015.

[37] A. M. Ionescu and H. Riel, "Tunnel field-effect transistors as energy-efficient electronic switches," *Nature,* vol. 479, pp. 329-337, 2011.

[38] D. Sarkar, X. Xie, W. Liu, W. Cao, J. Kang, and Y. Gong, "A subthermionic tunnel field-effect transistor with an atomically thin channel," *Nature,* vol. 526, pp. 91-95, 2015.

[39] R. Kappera, D. Voiry, S. Yalcin, B. Branch, G. Gupta, A. D. Mohite, *et al.*, "Phase-engineered low-resistance contacts for ultrathin MoS_2 transistors," *Nature Materials,* vol. 13, pp. 1128-1134, 2014.

[40] J. Yoon, W. Park, G. Y. Bae, Y. Kim, H. S. Jang, and Y. Hyun, "Highly flexible and transparent multilayer MoS_2 transistors with graphene electrodes," *Small,* vol. 9, pp. 3295-3300, 2013.

[41] H. Fang, M. Tosun, G. Seol, T. Chang, K. Takei, J. Guo, *et al.*, "Degenerate n-doping of few-layer transition metal dichalcogenides by potassium," *Nano Letters,* vol. 13, pp. 1991-1995, 2013.

[42] O. Lopez-Sanchez, D. Lembke, M. Kayci, A. Radenovic, and A. Kis, "Ultrasensitive photodetectors based on monolayer MoS_2," *Nature Nanotechnology,* vol. 8, pp. 497-501, 2013.

[43] W. Zhang, C. P. Chuu, J. K. Huang, C. H. Chen, and M. L. Tsai, "Ultrahigh-gain photodetectors based on atomically thin graphene-MoS_2 heterostructures," *Scientific Reports,* vol. 4, p. 3826, 2014.

[44] F. Alharbi, J. D. Bass, A. Salhi, A. Alyamani, H.-C. Kim, and R. D. Miller, "Abundant non-toxic materials for thin film solar cells: Alternative to conventional materials," *Renewable Energy,* vol. 36, pp. 2753-2758, 2011.

[45] M.-L. Tsai, S.-H. Su, J.-K. Chang, D.-S. Tsai, C.-H. Chen, C.-I. Wu, *et al.*, "Monolayer MoS_2 heterojunction solar cells," *ACS Nano,* vol. 8, p. 83178322, 2014.

[46] M. M. Furchi, A. Pospischil, F. Libisch, J. Burgdörfer, and T. Mueller, "Photovoltaic effect in an electrically tunable van der Waals heterojunction," *Nano Letters,* vol. 14, pp. 4785-4791, 2014.

[47] R. S. Sundaram, M. Engel, A. Lombardo, R. Krupke, A. C. Ferrari, P. Avouris, *et al.*, "Electroluminescence in single layer MoS_2," *Nano Letters,* vol. 13, pp. 1416-1421, 2013.

[48] Y. Ye, Z. Ye, M. Gharghi, X. Yin, H. Zhu, M. Zhao, *et al.*, "Exciton-related electroluminescence from monolayer MoS_2," in *2014 Conference on Lasers and Electro-Optics (CLEO)*, 2014, pp. 1-2.

[49] J. S. Ross, P. Klement, A. M. Jones, N. J. Ghimire, J. Yan, D. G. Mandrus, *et al.*, "Electrically tunable excitonic light-emitting diodes based on monolayer WSe_2 p-n junctions," *Nature Nanotechnology,* vol. 9, pp. 268-272, 2014.

[50] Y. Zhai, L. Mathew, R. Rao, D. Xu, and S. K. Banerjee, "High-performance flexible thin-film transistors exfoliated from bulk wafer," *Nano Letters,* vol. 12, pp. 5609-5615, 2012.

[51] D. Shahrjerdi and S. W. Bedell, "Extremely flexible nanoscale ultrathin body silicon integrated circuits on plastic," *Nano Letters,* vol. 13, pp. 315-320, 2013.

[52] T. Sekitani, T. Yokota, U. Zschieschang, H. Klauk, S. Bauer, K. Takeuchi, *et al.*, "Organic nonvolatile memory transistors for flexible sensor arrays," *Science,* vol. 326, pp. 1516-1519, 2009.

[53] A. Castellanos-Gomez, M. Poot, G. A. Steele, H. S. van der Zant, N. Agraït, and G. Rubio-Bollinger, "Elastic properties of freely suspended MoS_2 nanosheets," *Advanced Materials,* vol. 24, pp. 772-775, 2012.

[54] C. Lee, X. Wei, J. W. Kysar, and J. Hone, "Measurement of the elastic properties and intrinsic strength of monolayer graphene," *Science,* vol. 321, pp. 385-388, 2008.

[55] Y.-H. H. Lee, X.-Q. Q. Zhang, W. Zhang, M.-T. T. Chang, C.-T. T. Lin, K.-D. D. Chang, *et al.*, "Synthesis of large-area MoS_2 atomic layers with chemical vapor deposition," *Advanced Materials,* vol. 24, pp. 2320-2325, 2012.

[56] G. A. Salvatore, N. Münzenrieder, C. Barraud, and L. Petti, "Fabrication and transfer of flexible few-layers MoS_2 thin film transistors to any arbitrary substrate," *ACS Nano,* vol. 7, pp. 8809-8815, 2013.

[57] J. Pu, Y. Yomogida, K.-K. K. Liu, L.-J. J. Li, Y. Iwasa, and T. Takenobu, "Highly flexible MoS_2 thin-film transistors with ion gel dielectrics," *Nano Letters,* vol. 12, pp. 4013-4017, 2012.

[58] N. Petrone, I. Meric, J. Hone, and K. L. Shepard, "Graphene field-effect transistors with gigahertz-frequency power gain on flexible substrates," *Nano Letters,* vol. 13, pp. 121-125, 2013.

[59] H.-Y. Y. Chang, S. Yang, J. Lee, L. Tao, W.-S. S. Hwang, D. Jena, *et al.*, "High-performance, highly bendable MoS_2 transistors with high-k dielectrics for flexible low-power systems," *ACS Nano,* vol. 7, pp. 5446-5452, 2013.

[60] G.-H. H. Lee, Y.-J. J. Yu, X. Cui, N. Petrone, C.-H. H. Lee, M. S. Choi, *et al.*, "Flexible and transparent MoS_2 field-effect transistors on hexagonal boron nitride-graphene heterostructures," *ACS nano,* vol. 7, pp. 7931-7936, 2013.

[61] S. Das, R. Gulotty, A. V. Sumant, and A. Roelofs, "All two-dimensional, flexible, transparent, and thinnest thin film transistor," *Nano Letters,* vol. 14, pp. 2861-2866, 2014.

[62] M. Yi and Z. Shen, "A review on mechanical exfoliation for the scalable production of graphene," *Journal of Materials Chemistry A,* vol. 3, pp. 11700-11715, 2015.

[63] S. Roddaro, P. Pingue, V. Piazza, and V. Pellegrini, "The optical visibility of graphene: interference colors of ultrathin graphite on SiO_2," *Nano Letters,* vol. 7, pp. 2707-2710, 2007.

[64] Y. Hernandez, V. Nicolosi, M. Lotya, F. M. Blighe, Z. Sun, S. De, *et al.*, "High-yield production of graphene by liquid-phase exfoliation of graphite," *Nature Nanotechnology,* vol. 3, pp. 563-568, 2008.

[65] C. Knieke, A. Berger, M. Voigt, R. N. Taylor, J. Röhrl, and W. Peukert, "Scalable production of graphene sheets by mechanical delamination," *Carbon,* vol. 48, pp. 3196-3204, 2010.

[66] X. Chen, J. F. Dobson, and C. L. Raston, "Vortex fluidic exfoliation of graphite and boron nitride," *Chemical Communications,* vol. 48, p. 3703, 2012.

[67] X. Li, W. Cai, J. An, S. Kim, J. Nah, D. Yang, *et al.*, "Large-area synthesis of high-quality and uniform graphene films on copper foils," *Science,* vol. 324, pp. 1312-1314, 2009.

[68] Y. Gong, X. Zhang, G. Liu, L. Wu, and X. Geng, "Layer-controlled and wafer-scale synthesis of uniform and high-quality graphene films on a polycrystalline nickel catalyst," *Advanced Functional Materials,* vol. 22, pp. 3153-3159, 2012.

[69] I. Vlassiouk, M. Regmi, P. Fulvio, S. Dai, and P. Datskos, "Role of hydrogen in chemical vapor deposition growth of large single-crystal graphene," *ACS Nano,* vol. 5, pp. 6069-6076, 2011.

[70] J. Chen, Y. Guo, L. Jiang, Z. Xu, and L. Huang, "Near-equilibrium chemical vapor deposition of high-quality single-crystal graphene directly on various dielectric substrates," *Advanced Materials,* vol. 26, pp. 1348-1353, 2014.

[71] Q. Ji, J. Ju, H. Yuan, J. Shi, T. Gao, D. Ma, *et al.*, "Controlled growth of high-quality monolayer WS_2 layers on sapphire and imaging its grain boundary," *ACS Nano,* vol. 7, pp. 8963-8971, 2013.

[72] Y. Rong, Y. Fan, A. L. Koh, A. W. Robertson, K. He, and S. Wang, "Controlling sulphur precursor addition for large single crystal domains of WS_2," *Nanoscale,* vol. 6, pp. 12096-12103, 2014.

[73] Y. Gong, J. Lin, X. Wang, G. Shi, S. Lei, Z. Lin, *et al.*, "Vertical and in-plane heterostructures from WS_2/MoS^2 monolayers," *Nature Materials,* vol. 13, pp. 1135-1142, 2014.

[74] R. Beanland, J. S. Ross, P. Rivera, W. Yao, and D. H. Cobden, "Lateral heterojunctions within monolayer $MoSe_2$–WSe_2 semiconductors," *Nature Materials,* vol. 13, pp. 1096-1101, 2014.

[75] M.-Y. Li, Y. Shi, C.-C. Cheng, L.-S. Lu, Y.-C. Lin, H.-L. Tang, *et al.*, "Epitaxial growth of a monolayer WSe_2-MoS_2 lateral p-n junction with an atomically sharp interface," *Science,* vol. 349, pp. 524-528, 2015.

[76] A. L. Hsu, K. Zhang, H. Li, Z. Y. Juang, and M. S. Dresselhaus, "Synthesis of few-layer hexagonal boron nitride thin film by chemical vapor deposition," *Nano Letters,* vol. 10, pp. 4134-4139, 2010.

[77] P. B. Sorokin, C. Jin, J. Ni, A. G. Kvashnin, and D. G. Kvashnin, "Large scale growth and characterization of atomic hexagonal boron nitride layers," *Nano Letters,* vol. 10, pp. 3209-3215, 2010.

[78] C. Moura, R. S. Tare, R. O. C. Oreffo, and S. Mahajan, "Raman spectroscopy and coherent anti-Stokes Raman scattering imaging: prospective tools for monitoring skeletal cells and skeletal regeneration," *Journal of The Royal Society Interface,* vol. 13, p. 20160182, 2016.

[79] C. Lee, H. Yan, L. E. Brus, T. F. Heinz, J. Hone, and S. Ryu, "Anomalous lattice vibrations of single- and few-layer MoS2," *ACS Nano,* vol. 4, pp. 2695-2700, 2010.

[80] A. Molina-Sanchez and L. Wirtz, "Phonons in single-layer and few-layer MoS_2 and WS_2," *Physical Review B,* vol. 84, p. 155413, 2011.

[81] R. Muller and T. Kamins, *Device Electronics for Integrated Circuits. 3rd Edition.*: John Wiley & Sons: New York, 2002.

[82] X. Liang, B. A. Sperling, I. Calizo, G. Cheng, and C. A. Hacker, "Toward clean and crackless transfer of graphene," *ACS Nano,* vol. 5, pp. 9144-9153, 2011.

[83] Y. C. Lin, C. C. Lu, C. H. Yeh, C. Jin, and K. Suenaga, "Graphene annealing: how clean can it be?" *Nano Letters,* vol. 12, pp. 414-419, 2011.

[84] A. Ramasubramaniam, "Large excitonic effects in monolayers of molybdenum and tungsten dichalcogenides," *Physical Review B,* vol. 86, p. 115409, 2012.

[85] K. Kośmider and J. Fernández-Rossier, "Electronic properties of the MoS_2-WS_2 heterojunction," *Physical Review B,* vol. 87, p. 075451, 2013.

[86] A. Nourbakhsh, A. Zubair, M. S. Dresselhaus, and T. Palacios, "Transport properties of a MoS_2/WSe_2 heterojunction transistor and its potential for application," *Nano Letters,* vol. 16, pp. 1359-1366, 2016.

[87] X. Hong, J. Kim, S.-F. F. Shi, Y. Zhang, C. Jin, Y. Sun, *et al.*, "Ultrafast charge transfer in atomically thin MoS_2/WS_2 heterostructures," *Nature Nanotechnology,* vol. 9, pp. 682-686, 2014.

[88] F. Ceballos, M. Z. Bellus, H.-Y. Chiu, and H. Zhao, "Ultrafast charge separation and indirect exciton formation in a MoS_2–$MoSe_2$ van der Waals heterostructure," *ACS Nano,* vol. 8, pp. 12717-12724, 2014.

[89] X.-Q. Q. Zhang, C.-H. H. Lin, Y.-W. W. Tseng, K.-H. H. Huang, and Y.-H. H. Lee, "Synthesis of lateral heterostructures of semiconducting atomic layers," *Nano Letters,* vol. 15, pp. 410-415, 2015.

[90] A. Berkdemir, H. R. Gutiérrez, A. R. Botello-Méndez, N. Perea-López, A. Elías, C.-I. Chia, *et al.*, "Identification of individual and few layers of WS_2 using Raman Spectroscopy," *Scientific Reports,* vol. 3, p. 1755, 2013.

[91] L. Li, Y. Yu, G. J. Ye, Q. Ge, X. Ou, H. Wu, *et al.*, "Black phosphorus field-effect transistors," *Nature Nanotechnology,* vol. 9, pp. 372-377, 05//print 2014.

[92] V. Tran, R. Soklaski, Y. Liang, and L. Yang, "Layer-controlled band gap and anisotropic excitons in few-layer black phosphorus," *Physical Review B,* vol. 89, p. 235319, 2014.

[93] J. Qiao, X. Kong, Z.-X. Hu, F. Yang, and W. Ji, "High-mobility transport anisotropy and linear dichroism in few-layer black phosphorus," *Nature Communications,* vol. 5, 2014.

[94] H. O. H. Churchill and P. Jarillo-Herrero, "Two-dimensional crystals: Phosphorus joins the family," *Nature Nanotechnology,* vol. 9, pp. 330-331, 2014.

[95] H. Du, X. Lin, Z. Xu, and D. Chu, "Recent developments in black phosphorus transistors," *Journal of Materials Chemistry C,* vol. 3, pp. 8760-8775, 2015.

[96] F. Xia, H. Wang, and Y. Jia, "Rediscovering black phosphorus as an anisotropic layered material for optoelectronics and electronics," *Nature Communications,* vol. 5, p. 4458, 2014.

[97] X. Wang, A. M. Jones, K. L. Seyler, V. Tran, Y. Jia, H. Zhao, *et al.*, "Highly anisotropic and robust excitons in monolayer black phosphorus," *Nature Nanotechnology,* vol. 10, pp. 517-521, 2015.

[98] A. Jain and A. J. H. McGaughey, "Strongly anisotropic in-plane thermal transport in single-layer black phosphorene," *Scientific Reports,* vol. 5, p. 8501, 2015.

[99] Z.-Y. Ong, Y. Cai, G. Zhang, and Y.-W. Zhang, "Strong thermal transport anisotropy and strain modulation in single-layer phosphorene," *The Journal of Physical Chemistry C*, vol. 118, pp. 25272-25277, 2014.

[100] H. R. Chandrasekhar and U. Zwick, "Raman scattering and infrared reflectivity in GeSe," *Solid State Communications*, vol. 18, pp. 1509-1513, 1976.

[101] A. K. Singh and R. G. Hennig, "Computational prediction of two-dimensional group-IV mono-chalcogenides," *Applied Physics Letters*, vol. 105, p. 42103, 2014.

[102] Y. Hu, S. Zhang, S. Sun, M. Xie, and B. Cai, "GeSe monolayer semiconductor with tunable direct band gap and small carrier effective mass," *Applied Physics Letters*, vol. 107, p. 122107, 2015.

[103] R. Eymard and A. Otto, "Optical and electron-energy-loss spectroscopy of GeS, GeSe, SnS, and SnSe single crystals," *Physical Review B*, vol. 16, p. 1616, 1977.

[104] D. J. Xue, J. Tan, J. S. Hu, W. Hu, and Y. G. Guo, "Anisotropic photoresponse properties of single micrometer‐sized GeSe nanosheet," *Advanced Materials*, vol. 24, pp. 4528-4533, 2012.

[105] V. D. I. I. Dimitri, R. J. Patel, M. A. Hickner, and R. E. Schaak, "Single-crystal colloidal nanosheets of GeS and GeSe," *Journal of the American Chemical Society*, vol. 132, pp. 15170-15172, 2010.

[106] X. Zhang, J. Shen, S. Lin, J. Li, Z. Chen, W. Li, *et al.*, "Thermoelectric properties of GeSe," *Journal of Materiomics*, vol. 2, pp. 331-337, 2016.

[107] J. Wu, N. Mao, L. Xie, H. Xu, and J. Zhang, "Identifying the crystalline orientation of black phosphorus using angle resolved polarized raman spectroscopy," *Angewandte Chemie*, vol. 127, pp. 2396-2399, 2015.

[108] H. B. Ribeiro, M. A. Pimenta, C. J. S. de Matos, and R. L. Moreira, "Unusual angular dependence of the Raman response in black phosphorus," *ACS Nano*, vol. 9, pp. 4270-4276, 2015.

[109] J. Xia, X.-Z. Li, X. Huang, N. Mao, D.-D. Zhu, L. Wang, *et al.*, "Physical vapor deposition synthesis of two-dimensional orthorhombic SnS flakes with strong angle/temperature-dependent Raman responses," *Nanoscale*, vol. 8, pp. 2063-2070, 2015.

[110] R. Loudon, "The Raman effect in crystals," *Advances in Physics*, vol. 13, pp. 423-482, 1964.

[111] "Germanium: germanium selenide," ed. WebElements: https://www.webelements.com/compounds/germanium/germanium_selenide.html .